

Catalysis Science & Technology

Accepted Manuscript

This article can be cited before page numbers have been issued, to do this please use: K. G. Papanikolaou and M. Stamatakis, *Catal. Sci. Technol.*, 2021, DOI: 10.1039/D1CY00011J.



This is an Accepted Manuscript, which has been through the Royal Society of Chemistry peer review process and has been accepted for publication.

Accepted Manuscripts are published online shortly after acceptance, before technical editing, formatting and proof reading. Using this free service, authors can make their results available to the community, in citable form, before we publish the edited article. We will replace this Accepted Manuscript with the edited and formatted Advance Article as soon as it is available.

You can find more information about Accepted Manuscripts in the [Information for Authors](#).

Please note that technical editing may introduce minor changes to the text and/or graphics, which may alter content. The journal's standard [Terms & Conditions](#) and the [Ethical guidelines](#) still apply. In no event shall the Royal Society of Chemistry be held responsible for any errors or omissions in this Accepted Manuscript or any consequences arising from the use of any information it contains.

The Catalytic Decomposition of Nitrous Oxide and the $\text{NO} + \text{CO}$ Reaction over Ni/Cu Dilute and Single Atom Alloy Surfaces: First-principles Microkinetic Modelling

Konstantinos G. Papanikolaou and Michail Stamatakis*

Thomas Young Centre and Department of Chemical Engineering, University College London, Roberts Building, Torrington Place, London WC1E 7JE, UK

Abstract

The development of platinum group metal-free (PGM-free) catalysts, which can efficiently reduce pollution-causing emissions, is an important task for overcoming major environmental challenges. In particular, nitrogen oxides (NO_x) are major contributors to air pollution, being one of the culprits for smog and ozone depletion. In this work, we employ density functional theory (DFT) and microkinetic modelling to investigate the decomposition of N_2O and the $\text{NO} + \text{CO}$ reaction over two PGM-free Ni/Cu dilute alloys. On the first surface, Ni atoms are isolated on the host Cu(111), thereby forming a single atom alloy surface (i.e. Ni/Cu(111) SAA), while on the second, the same atoms are organised as Ni-Ni dimers (i.e. $\text{Ni}_2\text{Cu}(111)$). The same reactions are also simulated on pure Cu(111) (i.e. the host surface), and on Rh(111), which is used for benchmarking as Rh is a well-established PGM in emissions control catalysis. Our results suggest that the addition of trace amounts of Ni on Cu(111) may bring about significant improvement to the catalytic performance with regard to the catalytic decomposition of N_2O . Additionally, we determine that $\text{Ni}_2\text{Cu}(111)$ shows equivalent, or under some circumstances even better, performance as compared to Rh(111) for the $\text{NO} + \text{CO}$ reaction. This work contributes to the long-standing efforts toward the design of efficient PGM-free catalytic materials for the reduction of noxious gases.

*Corresponding Author. e-mail: m.stamatakis@ucl.ac.uk



1. Introduction

View Article Online
DOI: 10.1039/D1CY00011J

The catalytic reduction of nitric oxide (NO) and the decomposition of nitrous oxide (N₂O) are reactions of central significance for the prevention and mitigation of critical environmental problems. The emissions of these molecules are, to a large extent, associated with automobiles,¹ which are equipped with the so-called three way catalyst (TWC). TWCs are composed of a complex mixture of oxides (e.g. γ -Al₂O₃, BaO), whereon noble metals Rh, Pt and Pd are deposited and “undertake” the task of converting noxious gases (e.g. CO, NO, N₂O, C_xH_y) into environmentally acceptable products (i.e. N₂, H₂O, CO₂).

The catalytic reduction of NO by CO is a crucial reaction for controlling automobile emissions, and Rh is regarded as the most promising platinum group metal (PGM) to this end.¹ By and large, this is because Rh can activate the N–O bond at relatively low temperatures^{2–4} (the cleavage of this bond is in many cases the rate determining step of the NO + CO reaction^{5,6}), and also because of its high resistance to common poisons (e.g. sulphur).⁷ As a result, the mechanism and kinetics of the NO + CO reaction over Rh catalysts have been the subject of extensive research for several experimental,^{8–14} and theoretical studies.^{15–19}

Although Rh exhibits the best performance among other PGMs toward the reduction of NO, its high cost and limited resources are major shortcomings.¹ Unsurprisingly, these downsides have turned the attention of the catalysis community into the search of TWCs that are either PGM-free^{20–29} or utilise minimal amounts of PGMs.^{30–33} For example, Asakura et al. showed that a NiCu/Al₂O₃ alloy catalyst exhibits distinct catalytic behaviour compared to its Cu/Al₂O₃ and Ni/Al₂O₃ monometallic counterparts.²¹ The three materials were subject to alternating lean–rich cycles similar to those a TWC may experience during operation. The performance of the Ni–based catalyst deteriorated considerably within the first lean–rich cycle; the Cu–based catalyst was found to be susceptible to oxidation, thereby losing its activity within short time under lean conditions. By contrast, the NiCu/Al₂O₃ catalyst retained very high N₂ productivity for large time intervals even under lean conditions, and could



rapidly self-regenerate (i.e. transition from an oxide state to the corresponding metallic state) in the beginning of each rich period. The authors ascribed the self-regenerative property of NiCu/Al₂O₃ to the coexistence of Ni and Cu oxide species that remained in close contact at the end of lean periods.²¹ Tanaka and co-workers reported that the same bimetallic alloy supported on a Mg–Al mixed oxide serves as an efficient catalyst for hydrocarbon oxidation (i.e. another important reaction that happens over TWCs), under both reducing and oxidative atmospheres.²⁰ Xing et al. synthesised a highly dilute PdCu/Al₂O₃ catalyst, whereby Pd atoms were atomically dispersed on the Cu host.³³ This catalyst not only showed excellent stability during the NO + CO reaction, but also was able to convert fully NO to N₂ at relatively low temperatures (473 K).

In our recent theoretical work, we screened a number of dilute alloys for their performance on catalysing important “elementary” steps for the NO + CO reaction (e.g. direct NO dissociation, N₂ association and CO oxidation).⁴ According to our results, a Ni₂Cu alloy, where Ni atoms are organised as Ni–Ni dimers over the Cu host surface, is promising in activating the N–O bond and is capable of performing facile N₂ association.⁴ In particular, Ni₂Cu exhibited the best performance among the investigated bimetallic surfaces, and similar, or in many cases even better, performance than the PGMs in TWCs (i.e. Rh, Pd and Pt). Finally, we argued that this alloy might, in practice, exhibit bifunctional behaviour,³⁴ where Ni sites cleave N–O bonds, while Cu sites serve as the loci for the oxidation of CO.³⁵

In this paper, we employ density functional theory (DFT) and investigate in detail two very relevant reactions to the NO + CO chemistry over Ni/Cu(111) single atom and Ni₂Cu(111) dilute alloy surfaces; these are the formation and decomposition of N₂O*, in particular, NO* + N* ↔ N₂O* and N₂O* ↔ N₂* + O*, respectively, where * denotes an adsorbed species. Besides their relevance to the catalytic reduction of NO by CO (N₂O is an exhaust gas and an adduct of catalytic surface chemistry),³⁶ these reactions are also of general interest.³⁷ This is because N₂O is a potent greenhouse gas and an undesired by-product of large-scale processes like the production of adipic and nitric acid.³⁸ The same reactions



are studied over Rh(111), which is used for benchmarking, and also over Cu(111), which is the corresponding host metal surface. We identify different pathways for the activation of N_2O^* over all surfaces, and we demonstrate that the selectivity of this reaction can be tuned based on the size of the Ni cluster. Importantly, our calculations imply that the presence of small amounts of Ni on Cu(111) strengthens the binding of N_2O^* to the surface, thereby preventing its desorption and promoting its dissociation. Finally, using the obtained DFT energetics we parameterise a microkinetic model for the $NO + CO$ reaction over the four (111) surfaces. Our theoretical studies aim at providing a first assessment for the performance of the Ni/Cu dilute alloys toward the aforementioned reaction. These simulations reveal that the performance of $Ni_2Cu(111)$ is certainly superior compared to that of Cu(111) and closely comparable to that of Rh(111). On this basis, the present study highlights the potential of well-engineered Ni_2Cu alloys, which are composed of inexpensive and abundant metals, for emission control technologies.

2. Methods

Density Functional Theory: Periodic DFT calculations were performed using the Vienna *ab initio* simulation package (VASP) version 5.4.1.^{39,40} Exchange and correlation effects were treated with the optB86b–vdW functional,^{41,42} which captures van der Waals (vdW) interactions.^{43,44} The latter are important to our work and recent studies have shown that the inclusion of dispersion forces in DFT calculations may increase the binding strength of loosely bound adsorbates of the $NO + CO$ reaction (i.e. N_2O^* , CO_2^*) by as much as 0.7 eV.¹⁶ A kinetic energy cut-off of 400 eV was used for the plane wave basis set that was adopted to describe the wave functions of valence electrons. The interactions between core and valence electrons were modelled by the projector augmented wave (PAW) method.⁴⁵ The electronic wave function was converged to 10^{-7} eV, and the structures were relaxed until the forces on each atom were less than 0.01 eV/Å. The optB86b–vdW–computed lattice constants are 3.608 Å and 3.829 Å for Cu and Rh, respectively; these values agree well with the corresponding experimental values (3.596 Å and 3.793 Å for Cu and Rh, respectively).⁴⁶ The metal surfaces were modelled by a 3



× 3 cell with 5 layers, of which the two bottom ones were fixed at the corresponding lattice constant, thereby simulating the bulk of the material, while the three top layers and any adsorbate atoms were relaxed during geometry optimisation. The Brillouin zone was sampled using a 9 × 9 × 1 Monkhorst–Pack k–point mesh.⁴⁷ The adsorption energy of N₂O was computed based on the following equation:

$$E_{ads}(N_2O) = E_{tot}^{N_2O+Slab} - E_{tot}^{Slab} - E_{tot}^{N_2O(g)}, \quad (2)$$

where $E_{tot}^{N_2O+Slab}$, E_{tot}^{Slab} and $E_{tot}^{N_2O(g)}$ are the total DFT energies for a slab with an N₂O* thereon, a clean slab, and an N₂O molecule in the gas phase, respectively (the pertinent results are reported in Table 1).

The reported transition states were first approached using the dimer method,⁴⁸ fully converged with Newton's method, and verified by vibrational analyses, making sure that all the reported transition states had only one imaginary vibrational frequency. The reported activation barriers were computed as $E_a = E_{TS} - E_{IS}$, where E_{TS} and E_{IS} are the DFT energies of the transition and initial states, respectively. Vibrational frequencies were computed within the harmonic approximation where the energy of the system is expressed as a Taylor expansion that includes up to second order terms, and the second derivative was estimated within the finite–difference approximation with a displacement of 0.02 Å.

Microkinetic Modelling: The microkinetic model for the NO + CO reaction included 16 reaction steps for Cu(111), Ni/Cu(111) single atom alloy (SAA), and Ni₂Cu(111) surfaces and 14 reaction steps for Rh(111) – (see Table 2). On the monometallic surfaces there was only one site type, while in the bimetallic surfaces there were Cu and Ni sites, denoted as Cu* and Ni*, respectively. Therefore, for the latter surfaces, we define the “local” coverages as follows:

$$\theta_i^{(m)} = \frac{N_i^{(m)}}{N_{sites}^{(m)}}, \quad (3)$$

where $N_i^{(m)}$ is the number of molecules of adsorbate species i that are bound to sites of type m (either Cu* or Ni*); and $N_{sites}^{(m)}$ is the number of sites of type m . We further define the *total* coverage of adsorbate i , θ_i , as:



$$\theta_i = \sum_{m=1}^{N_{st}} x_m \theta_i^{(m)}, \quad (4)$$

View Article Online
DOI: 10.1039/D1CY00011J

where N_{st} is the total number of site types; the summation index m runs over these site types (for the bimetallic surfaces the two types are: Cu* and Ni*; for monometallic surfaces there is only one site type which can be either Cu* or Rh*); and x_m is the fraction of sites m on the surface, given as:

$$x_m = \frac{N_{sites}^{(m)}}{\sum_{l=1}^{N_{st}} N_{sites}^{(l)}}. \quad (5)$$

All reactions were considered reversible, and the forward/reverse rates were given by the typical mass-action law expressions used in microkinetic models, which contain the partial pressures of gas-phase species (considered as constants) and the surface coverages. The gas-phase species taken into account were NO, CO, N₂, CO₂, N₂O, while the surface species were O*, CO*, N*, NO*, CO₂*, N₂* and N₂O*, as well as the vacant site pseudo-species denoted as *. Regarding the N₂O* species, three different adsorption geometries were taken into account (see the next section). The transitions from one adsorption geometry to another could happen through *transformation reactions* that were included in the reaction mechanism (see R10 – R11 in Table 2). The forward rate for reaction j on site-type m is formulated as follows:

$$R_{fwd,j}^{(m)} = k_{fwd,j}^{(m)} \prod_{g \in R_j^{gas}} (P_g)^{-\nu_{gj}} \prod_{i \in R_j^{surf}} \left(\theta_i^{(\mu_{ij})} \right)^{-\nu_{ij}}. \quad (6)$$

In the above equation, R_j^{gas} is the set of gas-phase reactant species of reaction j ; P_g is the partial pressure of gas species g ; and ν_{gj} is the stoichiometric coefficient of that gas phase species in reaction j . By convention, stoichiometric coefficients are negative for reactants and positive for products; if a species does not appear in a certain reaction, the corresponding stoichiometric coefficient is zero. Moreover, R_j^{surf} is the set of surface reactant species of reaction j ; ν_{ij} is the stoichiometric coefficient



of that surface species i in reaction j ; and $\theta_i^{(\mu_{ij})}$ is the local coverage of surface species i on sites of type μ_{ij} . The latter term may or may not be equal to m , since, a reaction that is said to happen on site m (e.g. Ni*), may well involve another species adsorbed on a neighbouring site type (e.g. Cu*). For instance, when reaction R9 of Table 2 ($\text{NO}^* + \text{N}^* \leftrightarrow \text{N}_2\text{O}^* + *$) happens on a Ni site, NO^* is found on the Ni site, while N^* is on Cu; therefore, the rate would be:

$$R_{fwd,9}^{(\text{Ni}^*)} = k_{fwd,9}^{(\text{Ni}^*)} \theta_{\text{NO}^*}^{(\text{Ni}^*)} \theta_{\text{N}^*}^{(\text{Cu}^*)}.$$

For further information on the considered reactant configurations for events that involve two sites see Table S3 in the Supporting Information. Similarly, the reverse rate for reaction j on site-type m is formulated as follows:

$$R_{rev,j}^{(m)} = k_{rev,j}^{(m)} \prod_{g \in \mathbf{P}_j^{gas}} (P_g)^{v_{gj}} \prod_{i \in \mathbf{P}_j^{surf}} \left(\theta_i^{(\mu_{ij})} \right)^{v_{ij}}. \quad (7)$$

Note that \mathbf{P}_j^{gas} and \mathbf{P}_j^{surf} denote sets of products of reaction j , and the stoichiometric coefficients appear with their “original” positive signs, because of the convention mentioned earlier.

The rate constant calculations for the surface reactions ($k_{fwd,j}^{(m)}$ and $k_{rev,j}^{(m)}$) are calculated after invoking widely used transition state theory approximations. If a reaction cannot happen on a certain site, then

$k_{fwd,j}^{(m)} = k_{rev,j}^{(m)} = 0$. We further define the net rate of reaction j on site m as:

$$R_j^{(m)} = R_{fwd,j}^{(m)} - R_{rev,j}^{(m)}. \quad (8)$$

The coverage profiles over the investigated surfaces can now be obtained by solving a system of ordinary differential equations (ODEs) written as

$$\frac{d\theta_i^{(m)}}{dt} = \sum_{j=1}^{N_R} v_{ij} R_j^{(m)}, \quad (9)$$



where N_R is the total number of (reversible) reactions. The ODEs were solved in Matlab R2017a using the ode23s solver, which is capable of dealing with stiff equations. An important constraint that had to be satisfied is the *site conservation law*

$$\sum_{i=1}^{N_s} \sum_{m=1}^{N_{st}} x_m \theta_i^{(m)} = 1. \quad (10)$$

To calculate the rate constants of the reactions the following assumptions and approximations were adopted. Molecular adsorptions were assumed as non-activated events with a 2D gas as a transition state, where molecules retain translational and rotational degrees of freedom. Accordingly, the rate constants for molecular adsorptions were calculated using the Hertz–Knudsen equation assuming a sticking coefficient equal to unity (eq (11)):⁴⁹

$$k_{ads} = \frac{A_{st}}{\sqrt{2 \cdot \pi \cdot m_i \cdot k_B \cdot T}}, \quad (11)$$

where m_i is the mass of molecule i ; k_B is the Boltzmann constant; T is the temperature; and A_{st} is the effective area of the adsorption site. The pressure of gas phase–species is omitted in eq (11) because it is explicitly taken into account in eq (6) and eq (7). The rate constants for surface reactions and desorption events were calculated using the Eyring equation:⁵⁰

$$k_{fwd/rev,j}^{(m)} = \frac{k_B T}{h} \frac{Q^{TS}}{Q^{IS}} \exp\left(-\frac{E_{a,fwd/rev,j}^{(m)}}{k_B T}\right), \quad (12)$$

where h is the Planck's constant; Q^{TS} and Q^{IS} are the partition functions of the transition and initial states, respectively. The rate constants of surface reactions were calculated using the harmonic approximation, and therefore frustrated translations and rotations of surface species were treated as vibrations; under these circumstances, the partition function of an adsorbed state (either initial or transition state) is equal to the vibrational partition function (q_{vib}):



$$Q \approx q_{vib} = \prod_{k=1}^S \frac{e^{-\hbar\omega_k/2k_bT}}{1 - e^{-\hbar\omega_k/k_bT}}, \quad (13)$$

where S is the number of vibrational modes; ω_k is the angular frequency of the k^{th} normal mode of vibration; and \hbar is the reduced Planck's constant.

The net rates for N_2 and N_2O are calculated as follows:

$$R_{N_2,net} = \sum_{m=1}^{N_{st}} R_{R3,net}^{(m)}, \quad (14)$$

$$R_{N_2O,net} = \sum_{j=R5}^{R7} \sum_{m=1}^{N_{st}} R_{j,net}^{(m)}, \quad (15)$$

where $R_{j,net}^{(m)}$ is the net reaction rate of j on site m . Finally, the contribution of each elementary step to the total reaction rate was quantified using Campbell's degree of rate control (DRC) – (see eq (16)):^{51,52}

$$X_{RC,j}^{(m)} = \frac{k_j^{(m)}}{R_{N_2,net}} \left(\frac{\partial R_{N_2,net}}{\partial k_j^{(m)}} \right)_{K_l^{(n)}, k_l^{(n \neq m)}} = \left(\frac{\partial \ln R_{N_2,net}}{\partial \ln k_j^{(m)}} \right)_{K_l^{(n)}, k_l^{(n \neq m)}}, \quad (16)$$

where $X_{RC,j}^{(m)}$ is the DRC coefficient for reaction j on site m ; $R_{N_2,net}$ is the net reaction rate for the production of N_2 (eq. (14)) on site m (eq (8)); $K_l^{(n)}$ is the equilibrium constant of reaction $l = 1, \dots, N_R$ on site $m = 1, \dots, N_{st}$; $k_l^{(n \neq m)}$ are the rate constants for all other steps than j that take place on either Cu^* or Ni^* (the site other than m). The larger the absolute value of $X_{RC,j}^{(m)}$ the larger the influence of that reaction step to the overall reaction rate; also when $X_{RC,j}^{(m)} > 0$, the reaction is rate-limiting, whereas for $X_{RC,j}^{(m)} < 0$ the reaction is an inhibition step.



3. Results and Discussion

View Article Online
DOI: 10.1039/D1CY00011J

3.1. Adsorption of N₂O on Ni/Cu dilute alloy surfaces

Gas-phase nitrous oxide is a linear molecule ($C_{\infty V}$ symmetry) and a harmful by-product of industrial processes (e.g. nitric acid production). Its catalytic decomposition has been investigated over many transition metals, including Rh,⁵³ Cu,⁵⁴ Ru,⁵⁵ Pd,⁵⁶ Fe,⁵⁷ Ni,⁵⁸ Pt,⁵⁹ PdAu,⁶⁰ and PdCu.⁶¹ Here, we first examine the adsorption of nitrous oxide on Cu(111), Ni/Cu(111) SAA and Ni₂Cu(111) surfaces, but also on our “benchmarking surface” Rh(111).

It is known that N₂O* may adopt a number of different adsorption geometries upon its interaction with metal surfaces.^{56,62} Accordingly, we identify six stable adsorption geometries out of which four are displayed in Figure 1, while the full list is given in the first section of the Supporting Information. These four adsorption structures are important because they are adopted by N₂O* upon its decomposition to either to N₂* + O* or NO* + N* (see paragraphs 3.2 and 0), and are denoted as: $\eta 1-(N_t\{\text{top}\})$, $\eta 2-f(N_t\{\text{bridge}\}, N_c\{\text{top}\})$, $\eta 2-(N_t\{\text{top}\}, O\{\text{top}\})$, and $\eta 2-(N_t\{\text{hcp}\}, O\{\text{top}\})$ – (Figure 1). Since we will be referring often to the first three throughout this paper, we adopt the following abbreviations for them: $\eta 1$, $\eta 2NbNt$ and $\eta 2NtOt$, respectively.

The computed adsorption energies for the four geometries, along with the N–O (d_{N-O}) and N–N (d_{N-N}) bond distances are summarised in Table 1. We note that the most preferred N₂O* adsorption structure on Rh(111) is the $\eta 2NbNt$ mode ($E_{ads}(N_2O) = -0.83$ eV) – (Table 1). This type of adsorption can be considered as a weak chemisorption because: (1) the geometry of N₂O* deviates noticeably from the gas-phase geometry, which is linear; and (2) because the N–N bond is considerably elongated ($d_{N-N} = 1.14$ Å and 1.35 Å for gas-phase N₂O and $\eta 2NbNt$ N₂O*, respectively). The following most stable adsorption structures are the $\eta 1$ and $\eta 2NtOt$ with $E_{ads}(N_2O) = -0.71$ eV and $E_{ads}(N_2O) = -0.72$ eV, respectively. The former structure can be characterised as a strong physisorption owing to the unaffected geometry and bond lengths of $\eta 1$ N₂O* as compared to gas-phase N₂O ($d_{N-N} = 1.14$ Å and $d_{N-O} = 1.20$ Å for gas N₂O) – (Table 1).



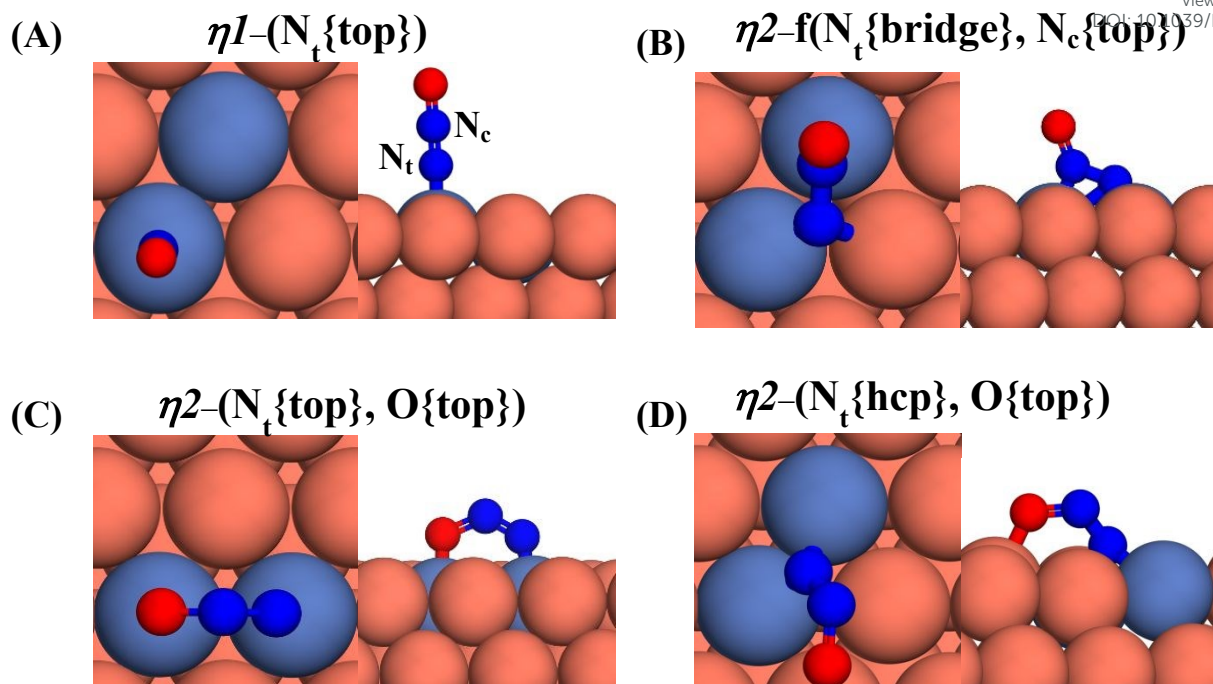


Figure 1. Top and side views of (A) $\eta 1-(N_t\{\text{top}\})$; (B) $\eta 2-f(N_t\{\text{bridge}\}, N_c\{\text{top}\})$; (C) $\eta 2-(N_t\{\text{top}\}, O\{\text{top}\})$ and (D) $\eta 2-(N_t\{\text{hcp}\}, O\{\text{top}\})$ adsorption structure. On the side view of (A) we highlight the terminal (N_t) and central (N_c) nitrogen atoms. Ni, Cu, N and O atoms are shown in purple, orange, blue and red, respectively. The adsorption geometries are shown over $Ni_2Cu(111)$, but they are representative for all surfaces.

The activation of the N—N bond in the $\eta 2NbNt$ structure can be elucidated by careful examination of the electronic structure of this geometry (Figure S2).⁶² Our density of states (DOS) analyses indicate that in $\eta 2NbNt$ the 2π and 3π orbitals of N_2O^* become broader as a result of their interaction with the metal states, whilst the same is not true for the $\eta 1$ structure where the same orbitals appear rather localised (Figure S2). The broadening of the 3π orbitals is indicative of electron back-donation, which in turn leads to the activation of the N—N bond. This result is in qualitative agreement with the work of Paul et al.⁶² where the authors, by means of DFT calculations using the PW91 functional, found that the $\eta 2NbNt$ and $\eta 1$ are ca. equally stable on Rh(111) ($E_{ads}(N_2O) = -0.35$ eV and $E_{ads}(N_2O) = -0.39$ eV, respectively). Moreover, our calculations suggest that N_2O^* is bound stronger by ca. 0.5 eV on Rh(111) compared to the work of Paul et al.⁶² and this discrepancy may be attributed to the inclusion of nonlocal electron correlation effects in our calculations.¹⁶



Table 1. Adsorption energies (in eV) and bond distances (in Å) for the N₂O* adsorption geometries over the investigated surfaces. The adsorption energies and bond distances that correspond to the most stable adsorption structure(s) for each surface are shown in bold. A dash indicates either that the adsorption structure is not stable on the specific surface or that it is not a minimum on the potential energy surface (i.e. there was an imaginary frequency in the vibrational analysis). For comparison: $d_{N-N} = 1.14$ Å and $d_{N-O} = 1.20$ Å for gas N₂O.⁶³

Adsorption Structure	Property	Rh(111)	Cu(111)	Ni/Cu(111) SAA	Ni ₂ Cu(111)
$\eta 1-(N_t\{\text{top}\})$ (denoted as $\eta 1$)	$E_{ads}(N_2O)$	-0.71	-0.21	-0.70	-0.68
	d_{N-O}	1.20	1.20	1.20	1.21
	d_{N-N}	1.15	1.15	1.15	1.15
$\eta 2-f(N_t\{\text{bridge}\}, N_c\{\text{top}\})$ (denoted as $\eta 2NbNt$)	$E_{ads}(N_2O)$	-0.83	+0.15	-0.43	-0.74
	d_{N-O}	1.22	1.23	1.23	1.23
	d_{N-N}	1.35	1.29	1.29	1.31
$\eta 2-(N_t\{\text{top}\}, O\{\text{top}\})$ (denoted as $\eta 2NtOt$)	$E_{ads}(N_2O)$	-0.72	-0.20	-0.53	-0.68
	d_{N-O}	1.33	1.28	1.30	1.32
	d_{N-N}	1.20	1.19	1.20	1.20
$\eta 2-(N_t\{\text{hcp}\}, O\{\text{top}\})$	$E_{ads}(N_2O)$	–	-0.25	-0.44	-0.73
	d_{N-O}	–	1.30	1.31	1.32
	d_{N-N}	–	1.27	1.25	1.27

We proceed by investigating the adsorption of N₂O* over Cu(111) and the Cu-based alloy surfaces where Ni atoms are either distributed as isolated atoms or as Ni–Ni dimers. In general, we find that N₂O* interacts weakly with Cu(111) (Table 1) and that the most stable adsorption geometries thereon are $\eta 2-(N_t\{\text{hcp}\}, O\{\text{top}\})$ and $\eta 1$ for which $E_{ads}(N_2O) = -0.25$ eV and -0.21 eV, respectively. Yet, the presence of a small amount of Ni on the surface layer of Cu(111) brings about drastic changes with regard to the binding strength of N₂O* (Table 1). Thus, the most stable adsorption geometry on the Ni/Cu(111) SAA surface is $\eta 1$ ($E_{ads}(N_2O) = -0.70$ eV), where the N_t atom of N₂O* interacts closely with the isolated Ni atom. By contrast, the $\eta 2NbNt$ and $\eta 2-(N_t\{\text{hcp}\}, O\{\text{top}\})$ are the most favourable adsorption modes for Ni₂Cu(111), with $E_{ads}(N_2O) = -0.74$ eV $E_{ads}(N_2O) = -0.73$ eV, respectively. Crucially, the corresponding adsorption processes are about 0.5 eV more exothermic than the $\eta 1$ and $\eta 2-(N_t\{\text{hcp}\}, O\{\text{top}\})$ modes on Cu(111), thereby highlighting the potential of the Ni/Cu dilute alloys



for the decomposition of N_2O^* . With this in mind, we examine the latter reaction over Cu(111) and the Cu-based surfaces.

3.2. N_2O^* formation and activation on Cu-based surfaces – the “conventional” reaction path

In order to verify the reliability of our data, we first perform calculations in relation to the activation of N_2O^* on the Rh(111) surface, and compare our results to those reported in previous theoretical works. The computed reaction pathway for the decomposition of N_2O^* to either $N_2^* + O^*$ or $NO^* + N^*$ is displayed in Figure S3. In this “conventional” reaction pathway the transformation of $NO^* + N^*$ to $N_2^* + O^*$ proceeds via the ηI adsorption structure (Figure S3), and our computed activation barriers are congruent with previously calculated values. For example, Paul et al.⁶² reported an activation barrier of 0.34 eV for the transformation of the $\eta 2NbNt$ structure to the ηI structure; this number is in good agreement with our computed barrier ($E_a = 0.38$ eV from state (4) to state (3) in Figure S3). Another example is the required barrier for the decomposition of the $\eta 2NbNt$ (state (1) in Figure S3) structure to $NO^* + N^*$. The values for this work and ref 62 are 0.36 eV and 0.41 eV, respectively. Consequently, we use our computational setup and study the decomposition of N_2O^* on Cu(111), Ni/Cu(111) SAA and $Ni_2Cu(111)$ surfaces.

Figure 2 (A) shows the “conventional” decomposition pathway for Cu(111), where the ηI structure “connects” the $NO^* + N^*$ and $N_2^* + O^*$ states. During the NO + CO reaction, the combination of NO^* and N^* species may result in the formation of N_2O^* , which ideally should be decomposed to $N_2^* + O^*$. Once formed, N_2O^* adopts the $\eta 2NbNt$ structure, and starting from this geometry on Cu(111) (state (1) in Figure 2 (A)), we realise that the formation of N_2^* and O^* is thermodynamically and kinetically favoured over the formation of NO^* and O^* . In particular, the decomposition of $\eta 2NbNt$ N_2O^* to $NO^* + O^*$ requires the traversing of a barrier of 0.94 eV, while the three barriers to be traversed for the formation of $N_2^* + O^*$ are only 0.14 eV, 0.06 eV and 0.06 eV. Yet, we conjecture that Cu(111) will be susceptible to the production of N_2O during the NO + CO reaction. This is because



of the following reasons: (1) N_2O^* can be formed from NO^* and N^* species with a relatively small kinetic barrier of 0.44 eV (Figure 2 (A)); once N_2O^* is formed from NO^* and N^* in the $\eta 2NbNt$ structure (state (1) in Figure 2 (A)), its desorption is the most probable scenario (Table 1); and (3) even in the $\eta 1$ and $\eta 2NiOt$ geometries, N_2O^* binds weakly on Cu(111) and its desorption will be proceeding at considerable rates even at moderate reaction temperatures.

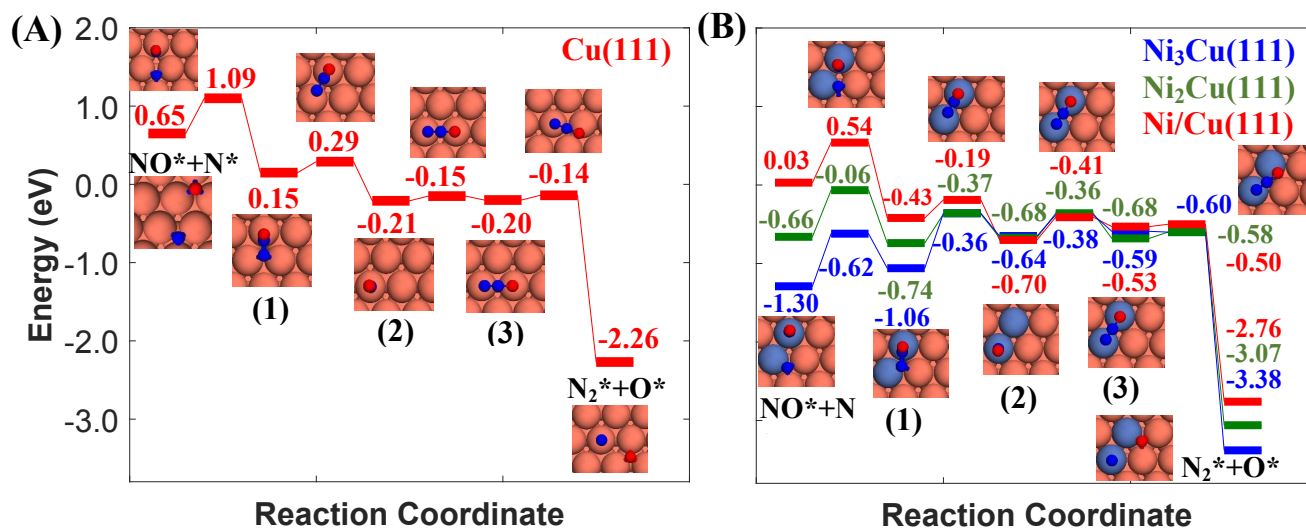


Figure 2. Reaction path for the decomposition of N_2O^* to $NO^* + N^*$ or $N_2^* + O^*$ over (A) Cu(111) surface; (B) Ni/Cu(111) SAA, $Ni_2Cu(111)$ and $Ni_3Cu(111)$ surfaces. The numbering of the adsorbed configurations of N_2O is as follows: (1) $\eta 2NbNt$, (2) $\eta 1$ and (3) $\eta 2NiOt$. The zero level corresponds to infinitely separated (and thus non-interacting) N_2O molecule and clean slab. States without any labelling are transition states. Side views of the different states are shown in the Supporting Information. Ni, Cu, O and N atoms are shown in purple, orange, red and blue, respectively.

On the contrary, we find that the decomposition of N_2O^* may be significantly promoted by embedding one or two Ni atoms on Cu(111), thereby forming a single atom alloy or a dilute alloy surface,^{64–71} where in the latter case Ni atoms are organised as dimers or trimers. We note that *ab initio* Monte Carlo simulations predict that small Ni clusters (e.g. Ni–Ni dimers) are abundant in Ni/Cu dilute alloy surfaces under vacuum conditions, while their thermodynamic stability can be further enhanced by exposing the alloy surface to CO at a range of partial pressures that lead to dopant fractional coverages less than 1.⁷² The computed desorption energies for $\eta 2NbNt$ N_2O^* (state (1) in Figure 2 (B)) on Ni/Cu(111) SAA and $Ni_2Cu(111)$ are 0.43 eV and 0.74 eV, respectively. By considering this adsorption structure as the starting point, we note that the transformation of N_2O^* to structure $\eta 1$ (i.e.



state (2)) and $\eta 2NiOt$ (i.e. state (3)), and the decomposition of the latter to $N_2^* + O$ would generally traverse small barriers, which are always less than 0.30 eV and 0.40 eV for Ni/Cu(111) SAA and Ni₂Cu(111), respectively. Thus, $\eta 2NbNt$ N₂O* (state (1)) would prefer to decompose to $N_2^* + O^*$, than desorb to the gas phase (Figure 2 (B)).

The exothermic adsorption of $\eta 2NbNt$ N₂O* (i.e. the first adopted structure after N₂O* formation from NO* and N*) will, to certain extent, prevent the N₂O* desorption to the gas phase. This will increase the probability of “trapping” N₂O* to the catalyst surface and therefore the probability for its decomposition. Moreover, even stronger $\eta 2NbNt$ N₂O* binding should be expected on Ni–Ni dimers and Ni single atoms that are embedded on more open surfaces than the densely packed (111) and on undercoordinated sites that can be found in catalytic nanoparticles.

Another point that merits consideration is that the selectivity toward the decomposition products (NO* + N* or N₂* + O*) can be altered by tuning the size of the Ni cluster. To better illustrate this point, we present the corresponding N₂O* decomposition pathway over a Cu(111) with an embedded Ni trimer (Ni₃Cu(111) in Figure 2 (B)). Interestingly, the kinetic barrier for the formation of the $\eta 2NbNt$ geometry (state (1) in Figure 2 (B)) from NO* and N* increases monotonically at increasing size of the Ni cluster ($E_a = 0.51$ eV, 0.60 eV and 0.68 eV for Ni/Cu(111) SAA, Ni₂Cu(111) and Ni₃Cu(111), respectively). The opposite is true for the reverse reaction (i.e. $\eta 2NbNt$ N₂O* to NO* + N*) for which $E_a = 0.97$ eV, 0.68 eV and 0.44 eV for Ni/Cu(111) SAA, Ni₂Cu(111) and Ni₃Cu(111), respectively. This result underlines the importance of developing ways to control the architecture of dilute alloy surfaces and former studies discuss that this may be achieved under reactive conditions.^{72–75}

N₂O formation and activation on Cu–based surfaces – an alternative reaction path

Besides the “conventional” route for the decomposition of N₂O* (Figure 2), we have identified an alternative reaction pathway which, to the best of our knowledge, has not been reported before. This path exists only on Cu(111) and on the Ni/Cu dilute alloy surfaces. The decomposition of N₂O* to



$N_2^* + O^*$ happens without transformation to the $\eta 1$ structure as in the conventional pathway. In contrast, in this pathway the two decomposed states (i.e. $NO^* + N^*$ and $N_2^* + O^*$) are “connected” via the $\eta 2-(N_t\{fcc\}, O\{top\})$ adsorption structure (this is as Figure 1 (D) but over an fcc site; the two adsorption structures exhibit the same binding strength $-E_{ads}(N_2O) = -0.74$ eV for $Ni_2Cu(111)$). After performing a number of test simulations, we could not identify the same path on $Rh(111)$, and this might explain why it was not reported in previous studies.⁶²

For all the Cu-based surfaces, Figure 3 shows that $\eta 2NbNt N_2O^*$ is formed in the same way as in the reaction path of Figure 2. Then the $\eta 2NbNt N_2O^*$ rotates around the axis of the N–N bond, thereby bringing the more electronegative O closer to the surface. Interestingly, once O is closer to the $Ni/Cu(111)$ SAA, the N–O bond is immediately cleaved and the kinetic barrier for this process is only 0.23 eV (Figure 3 (B)). The ease by which the N–O is broken over the Ni/Cu SAA surface may be associated with the sharp and narrow distribution of the electron density of the single Ni atom close to the Fermi level,^{4,76} and it is expected that back-donation to the 3π antibonding orbital of N_2O^* enables the facile activation of the N–O bond.

By contrast, the decomposition of N_2O^* to N_2^* and O^* is taking place through the $\eta 2-(N_t\{fcc\}, O\{top\})$ geometry (state (2) and (3) in Figure 3 (A) and (C), respectively) over $Cu(111)$ and $Ni_2Cu(111)$. The intervening barriers between the $\eta 2NbNt$ and $N_2^* + O^*$ states are small (≤ 0.23 eV). Irrespective of these low kinetic barriers, $Cu(111)$ is still expected to be prone to releasing N_2O^* to the gas phase given the generally weak $N_2O^*-Cu(111)$ interaction (Figure 3 (A)). The same is not true for $Ni_2Cu(111)$ where the N_2O^* desorption energy is in the range of 0.65 eV – 0.74 eV, while the kinetic barriers that lead to $N_2^* + O^*$ are between 0.06 eV and 0.23 eV (Figure 3 (C)). Given the similar energetics between the pathway of Figure 3 and the “conventional” one, we conclude that both of them need to be considered in the reaction mechanism of the $NO + CO$ reaction. Importantly, the existence of alternative N_2O^* decomposition paths may provide an explanation of the high selectivity to N_2 exhibited by dilute Cu-based alloys.³³



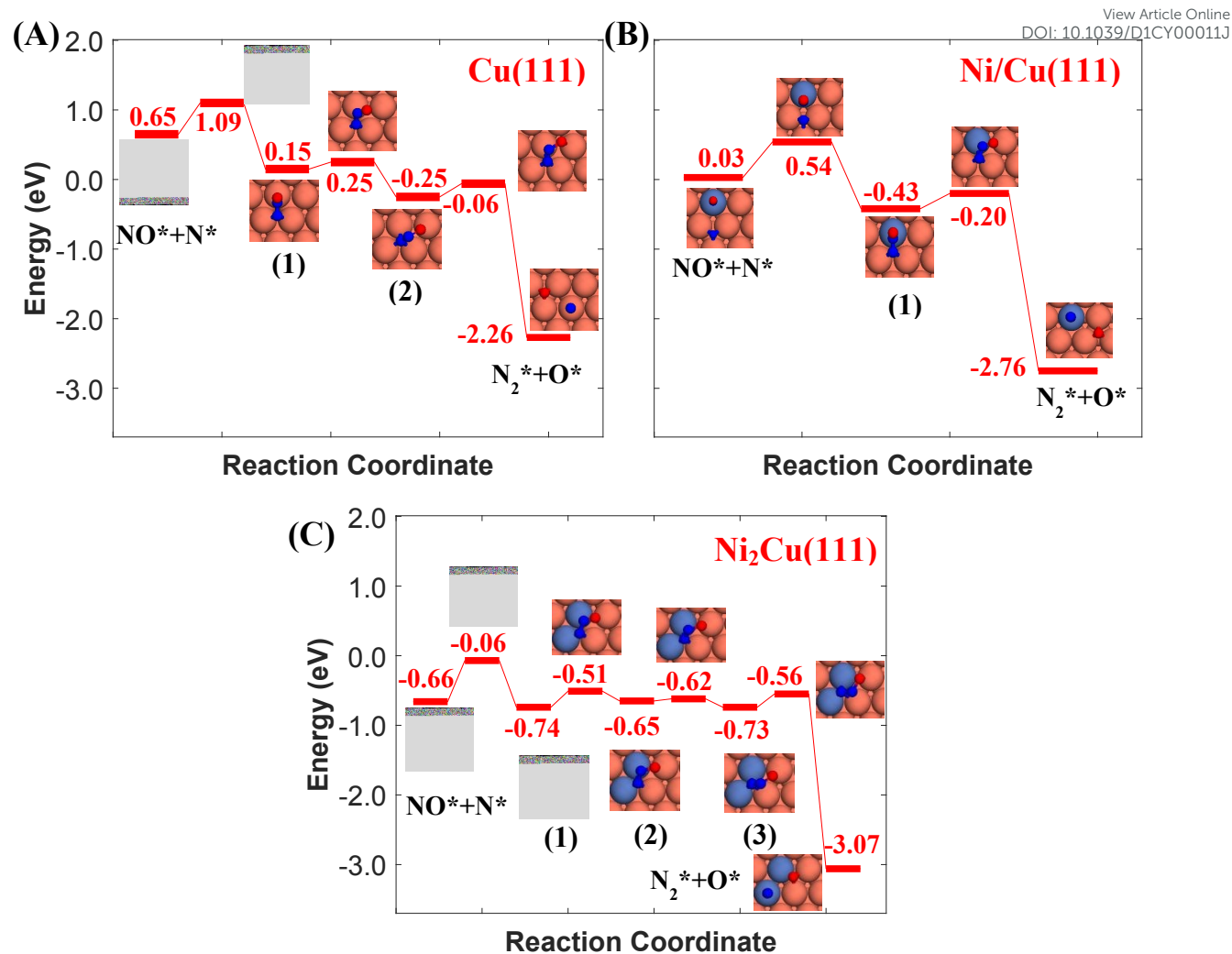


Figure 3. A second reaction path for the decomposition of N_2O^* on (A) Cu(111); (B) Ni/Cu(111) SAA and (C) $Ni_2Cu(111)$. State (1) corresponds to a η^2NbNt structure in all panels. The $\eta^2-(N_t\{fcc\}, O\{top\})$ structure is state (2) and state (3) in panels (A) and (C), respectively. The zero level corresponds to infinitely separated (and thus non-interacting) N_2O molecule and clean slab. States without any labelling are transition states. Side views of the different states are shown in the Supporting Information. Ni, Cu, O and N atoms are shown in purple, orange, red and blue, respectively.

3.3. N_2O formation and activation on Cu-based surfaces through the formation of $(NO)_2^*$

Thus far, the formation of nitrous oxide was assumed to proceed through the coupling of NO^* and N^* species (Figure 2 and Figure 3). NO^* is of course the product of the molecular adsorption of gas-phase nitric oxide. On the other hand, the existence of N^* species implies prior scission of the N–O bond. In general, low-index coinage metal surfaces exhibit large kinetic barriers for the direct dissociation of NO^* ($E_a = 1.57$ eV for Cu (111) and (100), and $E_a > 2.5$ eV for Ag and Au (111) and



(100) surfaces),⁴ thereby being ineffective at activating the N—O bond of NO*. Yet, they are known to be active for the reduction of NO, which is mainly converted to N₂O. The activity of coinage metal surfaces is ascribed to the formation of NO* dimer species (i.e. (NO)₂*) whose N—O bonds are more easily activated than those of monomeric NO*.^{33,54,77–79} This species is formed owing to vdW interactions between neighbouring NO* species,⁸⁰ and may be observed even at relatively low NO* coverages over Cu(111).⁴³ On the contrary, our calculations indicate that NO* is adsorbed as a monomer on Rh(111) and this is corroborated by near edge X-ray absorption fine structure spectroscopy.⁸¹

The most energetically favoured adsorption structure of NO* on Cu(111) is an N-down geometry where the N—O bond axis is perpendicular to the surface, and N is above an fcc hollow site ($E_{ads}(NO) = -1.55$ eV).⁴ A stable NO dimer is formed when two NO* species are adsorbed on adjacent fcc sites (NO* + NO* state in Figure 4 (A)). We note that in the relaxed geometry of this state, the O atoms of the neighbouring nitric oxide adspecies are slightly tilted towards each other (Figure 4 (A)). The thermodynamic stability of this configuration has been confirmed by other DFT studies, as well as in scanning tunnelling microscopy experiments.^{43,80} The two neighbouring NO* species can be converted to N₂O* (with an $\eta 1$ structure) and O* (see state (1) in Figure 4 (A)). This is happening *via* a transition state where one of the two NO* adsorbates bends down to the Cu(111) surface, while the other is slightly lifted (Figure 4 (A)). Once $\eta 1$ N₂O* is formed, its decomposition occurs in the same way as in Figure 2 (A), namely through the formation of the $\eta 2NiOt$ structure. We note that the structure of the (NO)₂* transition state, and the computed barrier for the scission of the N—O bond *via* the (NO)₂* precursor ($E_a = 0.84$ eV) are in excellent agreement with the DFT calculations by Bogicevic and Hass ($E_a = 0.82$ eV),⁵⁴ thereby furnishing further evidence for the reliability of our calculations.

We continue by investigating the same reaction pathway over the Ni/Cu(111) SAA and Ni₂Cu(111) surfaces. Our calculations show that the formation of N₂O* *via* the dimerization route is indeed possible over small Ni clusters. In contrast to Cu(111), on these dilute alloys (NO)₂* adopts a flat



geometry parallel to the surfaces in the transition state, and the computed kinetic barriers are 1.27 eV and 1.30 eV for Ni/Cu(111) SAA and Ni₂Cu(111), respectively (Figure 4 (A) and (B)). These values are higher than the computed barrier for Cu(111) – ($E_a = 0.84$ eV), and this may be attributed to the extra energy cost required for bending down both NO* species. Nevertheless, they are lower than or equal to the corresponding kinetic barriers for the direct dissociation of NO* ($E_a = 1.47$ eV and 1.30 eV for Ni/Cu(111) SAA and Ni₂Cu(111), respectively).⁴ Therefore, the formation and decomposition of N₂O* through dimerization is another pathway that should be included in the reaction mechanism of the NO + CO reaction over the Cu-based alloy surfaces.

To elucidate the effect of the Ni cluster size to the formation rate of $\eta 1$ N₂O* and O* via the (NO)₂* intermediate, we perform additional calculations for the Ni₃Cu(111) surface (Figure S5). On this surface, we compute $E_a = 1.77$ eV and $E_a = 1.37$ eV for the splitting of the N–O bond via dimerization (Figure S5) and via the direct NO* dissociation,⁴ respectively. Additionally, we note that on Ni dimers and trimers the formed $\eta 1$ N₂O* can be transformed to the $\eta 2 NtOt$ (state (3) in Figure 4 (C) for Ni₂Cu), and decompose to N₂* + 2O* only after O* spillover to Cu(111). The barrier for O* diffusion from a mixed hollow site to a Cu hollow site over Ni₂Cu(111) (from state (1) to state (2) in Figure 4 (C)) is 0.61 eV. Therefore, this extra energy cost in conjunction with the large kinetic barrier for the scission of the N–O bond of (NO)₂* render the decomposition of N₂O* through the dimerization pathway less likely on Ni clusters with more than two Ni atoms.

View Article Online
DOI: 10.1039/D1CY00011J



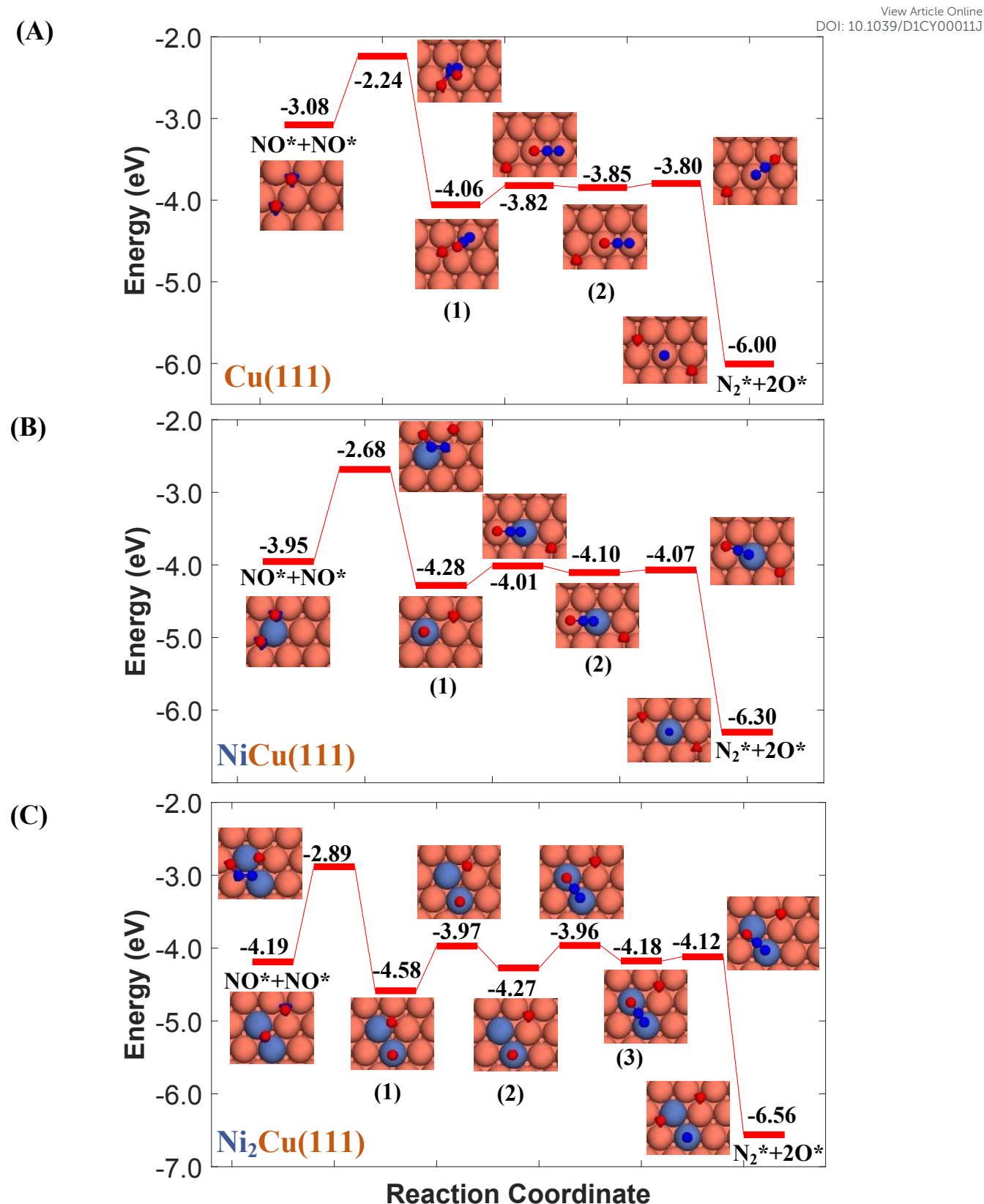


Figure 4. Reaction pathway for the formation and decomposition of N_2O^* via $(NO)_2^*$ for (A) Cu(111); (B) Ni/Cu(111) SAA; and (C) $Ni_2Cu(111)$. The zero level corresponds to two non-interacting gas-phase NO molecules and a clean slab. States without any labelling are transition states. Side views of the different states are shown in the Supporting Information. Ni, Cu, O and N atoms are shown in purple, orange, red and blue, respectively.



3.4. The microkinetics of the NO + CO reaction over Ni/Cu dilute alloys

View Article Online

DOI: 10.1039/D1CY00011J

Using the computed energetics for the decomposition of N_2O^* in conjunction with previous results for the formation of N_2^* , CO^* oxidation and NO^* decomposition over Ni/Cu surfaces,⁴ we parameterise a microkinetic model for the NO + CO reaction. Our studies include one site type for Cu(111) and Rh(111) surfaces, and two site types for the bimetallic surfaces (see section 2). The goal is a preliminary assessment of the catalytic performance of the Ni/Cu dilute alloys and a comparison to Cu(111) and Rh(111). Accordingly, the microkinetic simulations are performed in the absence of adsorbate–adsorbate interactions,^{82–85} whose effects on the coverage profiles, and consequently on the catalytic performance of the Cu–based surfaces may be important (this is part of ongoing research). Regarding the bimetallic surfaces, we assume that Ni^* species (single atoms or dimers) can be occupied by one adspecies (e.g. CO^*), which can react with another adspecies on a Cu site (e.g. O^*) and form a product on the Ni site (e.g. CO_2^*). Such events are treated as reactions that take place on the dopant site, and follow the energetics computed over the Ni site of the Ni/Cu surfaces. On the contrary, the Cu(111) energetics are used if the reaction involves two adspecies that are both on Cu sites (Table S3). Despite their simplicity, such microkinetic models are capable of capturing the salient features of experimental trends,⁸⁶ providing mechanistic insights,⁸⁷ and aiding in the identification of the active site during catalysis.^{88,89}

The NO + CO reaction mechanism is composed of 16 reversible reaction steps, shown in Table 2 along with their forward and reverse barriers. For all simulations the total pressure is set to 16.0 Torr with $P_{NO} = P_{CO} = 8.0$ Torr, thereby replicating the experimental conditions of Belton and co-workers.¹³ At this point, we note that the dissociative desorption of O_2 and the formation of NO_2^* are reactions through which O^* may be removed from the surface and they could be included in the microkinetic model. However, both of them exhibit very high kinetic barriers, and on this basis are excluded from the reaction mechanism. For example, the computed barrier for the O_2^* association reaction on Cu(111) is 2.10 eV, while the barrier for the reverse process is just 0.16 eV (see section 7 in the



Supporting Information); these values are in reasonable agreement with former DFT calculations.⁹⁰

Along the same lines, we find that the dissociation of NO_2^* to $\text{NO}^* + \text{O}^*$ is significantly more facile than its formation and its desorption (see section 7 in the Supporting Information).

We first simulate the $\text{NO} + \text{CO}$ reaction on $\text{Rh}(111)$. The *total* coverages of the surface species and the DRC analysis for this surface are shown in Figure 5 (A). The coverage profiles reveal that the catalyst surface is saturated with NO^* species up to temperatures of 1000 K. Under these conditions, the high surface coverage gives rise to steric hindrance effects, which prevent the dissociation of NO^* . This behaviour has been reported in the experimental work of Herman et al., and is in qualitative agreement with the fact that $\text{Rh}(111)$ is catalytically active only at temperatures higher than 625 K.¹³ Moreover, our model predicts that surface sites are freed up by NO adspecies only at $T > 1000$ K; this high “T threshold” can be attributed to (1) the absence of the repulsive NO^*-NO^* in our microkinetics (see Figure S4 in the Supporting Information); and (2) the very strong $\text{NO}^*-\text{Rh}(111)$ interaction predicted by the optB86b–vdW functional. In particular, NO^*-NO^* interactions may contribute to the reduction of the surface coverage, and in turn, this will generate free sites whereon the dissociation of NO^* can happen at lower temperatures than those predicted by our model.^{91,92} Regarding the second point, we find that the most stable adsorption site for NO^* on $\text{Rh}(111)$ is hcp, in line with previous computational and experimental works.^{5,93,94} However, we compute $E_{ads}(\text{NO}) = -2.85$ eV, which is larger than the PW91 values of Mavrikakis et al.⁹⁴ (-2.39 eV – 2×2 cell) and of González et al.⁹³ (-2.62 eV – 3×3 cell). Unfortunately, at coverages of 0.11 ML, like in our DFT calculations, accurate experimental measurement of $E_{ads}(\text{NO})$ is challenging because of the tendency of NO^* to dissociate on $\text{Rh}(111)$.⁹⁴ The reduction of the NO^* surface coverage gives rise to the formation of N^* and O^* at $T > 1000$ K. The accumulation of N^* species in the temperature range of 1000 K – 1200 K, is associated with the inefficiency of $\text{Rh}(111)$ in forming $\eta^2\text{NbNi N}_2\text{O}^*$ (R9, $E_a = 1.50$ eV) and N_2^* (R16, $E_a = 1.85$ eV) – (Table 2). Both reaction steps are rate-limiting with a positive DRC coefficient ($0.19 \leq X_{DRC,R9} \leq 0.30$) between 1100 K and 1300 K (Figure 5 (A)). Along the same lines, the build-up of O^* is



ascribed to the moderate activation barrier for the CO* oxidation reaction ($E_a = 1.17$ eV, R14 in Table

View Article Online
DOI: 10.1039/C1CY00011J

2), which is the only reaction that exhibits a reasonable activation barrier for the removal of O* from the surface.

Table 2. Reaction mechanism for the NO + CO reaction, and the corresponding forward (E_{fwd}) and reverse (E_{rev}) barriers (in eV). All reactions are treated as reversible, and dashes mean that the corresponding reaction does not take place on the catalyst surfaces. R1–R7 correspond to molecular adsorptions/desorptions; R8–R16 are surface reactions from which R10 and R11 are N₂O* transformation reactions.

Reaction & Reaction Number	Rh(111)		Cu(111)		Ni/Cu(111) SAA		Ni ₂ Cu(111)		
	E_{fwd}	E_{rev}	E_{fwd}	E_{rev}	E_{fwd}	E_{rev}	E_{fwd}	E_{fwd}	
NO _(g) + * ↔ NO*	(R1)	0.00	2.87	0.00	1.55	0.00	2.10	0.00	2.65
CO _(g) + * ↔ CO*	(R2)	0.00	2.20	0.00	0.78	0.00	1.51	0.00	1.71
N _{2(g)} + * ↔ N ₂ *	(R3)	0.00	0.79	0.00	0.15	0.00	0.79	0.00	0.77
CO _{2(g)} + * ↔ CO ₂ *	(R4)	0.00	0.27	0.00	0.30	0.00	0.28	0.00	0.37
N ₂ O _(g) + * ↔ N ₂ O* η_{2NbNt}	(R5)	0.00	0.83	0.00	0.00	0.00	0.43	0.00	0.74
N ₂ O _(g) + * ↔ N ₂ O* η_{2NiOt}	(R6)	0.00	0.72	0.00	0.20	0.00	0.53	0.00	0.68
N ₂ O _(g) + * ↔ N ₂ O* η_l	(R7)	0.00	0.71	0.00	0.21	0.00	0.70	0.00	0.68
NO* + * ↔ N* + O*	(R8)	1.42	2.03	1.57	1.43	1.47	1.43	1.30	1.24
NO* + N* ↔ N ₂ O* $\eta_{2NbNt} + *$	(R9)	1.50	0.40	0.44	0.94	0.51	0.45	0.60	0.68
N ₂ O* $\eta_{2NbNt} \leftrightarrow$ N ₂ O* η_l	(R10)	0.46	0.30	0.14	0.56	0.24	0.50	0.37	0.31
N ₂ O* $\eta_l \leftrightarrow$ N ₂ O* η_{2NiOt}	(R11)	0.24	0.40	0.06	0.05	0.29	0.12	0.32	0.32
N ₂ O* $\eta_{2NiOt} + * \leftrightarrow$ N ₂ * + O*	(R12)	0.07	2.54	0.05	2.12	0.03	2.26	0.09	2.48
N ₂ O* $\eta_{2NbNt} + * \leftrightarrow$ N ₂ * + O*	(R13)	—	—	0.19	2.20	0.23	2.56	0.23	2.51
CO* + O* ↔ CO ₂ * + *	(R14)	1.17	0.41	0.48	1.22	0.71	0.60	0.88	0.48
NO* + NO* ↔ N ₂ O* $\eta_l + O*$	(R15)	—	—	0.84	1.82	1.27	1.60	1.30	1.69
N* + N* ↔ N ₂ *	(R16)	1.85	2.14	0.64	3.6	0.88	3.40	0.62	2.81



The corresponding coverage profiles and DRC analysis for Cu(111) are displayed in Figure 5 (B). Cu(111) exhibits rather different behaviour than Rh(111). In particular, at $T < 350$ K all surface sites are occupied by NO^* , but at $T > 350$ K there is a sharp increase in the coverage of the O^* species. This sharp transition is attributed to the activation of the N–O bond *via* the NO^* dimerization reaction ($E_a = 0.84$ eV) – (R15 in Table 2), which converts 2NO^* to O^* and $\eta/1 \text{N}_2\text{O}^*$. The catalyst surface remains fully covered by O^* within the temperature range of 420 K – 900 K. Accordingly, our DRC analysis shows that under these conditions, the oxidation of CO^* controls the reaction rate, and that the NO^* dimerization is an inhibiting step as it adds more O^* onto the surface (Figure 5 (B)).

The last two coverage profiles shown in Figure 5 (panels (C) and (D)) are those for the Ni/Cu alloy surfaces. These surfaces contain a total of 10,000 sites, out of which 9,000 are Cu sites (Cu^*) and 1,000 are Ni sites (Ni^*). The coverage profiles are very similar on both cases, and indicate that Cu^* sites are covered with O^* up to ca. 900 K (similar to Cu(111)), while Ni^* sites are poisoned by NO^* . A disparity between the two surfaces is seen between 1000 K and 1500 K, where we observe a small build-up of N^* over $\text{Ni}_2\text{Cu}(111)$ only (Figure 5 (C) and (D)). The presence of N^* on the latter surface is indicative of the direct NO^* dissociation (R8, $E_a = 1.30$ eV – Table 2), which happens to a smaller extent on the SAA surface (R8, $E_a = 1.47$ eV – Table 2). Markedly, the N^* accumulation remains at low levels thanks to the efficiency of $\text{Ni}_2\text{Cu}(111)$ in forming N_2^* and $\eta/2\text{NbNt} \text{N}_2\text{O}^*$ (Table 2). The latter can either decompose to $\text{N}_2^* + \text{O}^*$ (R10, R11, R12 and R13) or desorb (R5).

Next, we examine the activity and selectivity to N_2 of the four surfaces. The latter metric is computed as

$$S_{\text{N}_2/\text{N}_2\text{O}} = \frac{R_{\text{N}_2,\text{net}}}{R_{\text{N}_2,\text{net}} + R_{\text{N}_2\text{O},\text{net}}}, \quad (17)$$

$R_{\text{N}_2,\text{net}}$ and $R_{\text{N}_2\text{O},\text{net}}$ are the net reaction rates for N_2 and N_2O , respectively (see eq (14) and eq (15)).



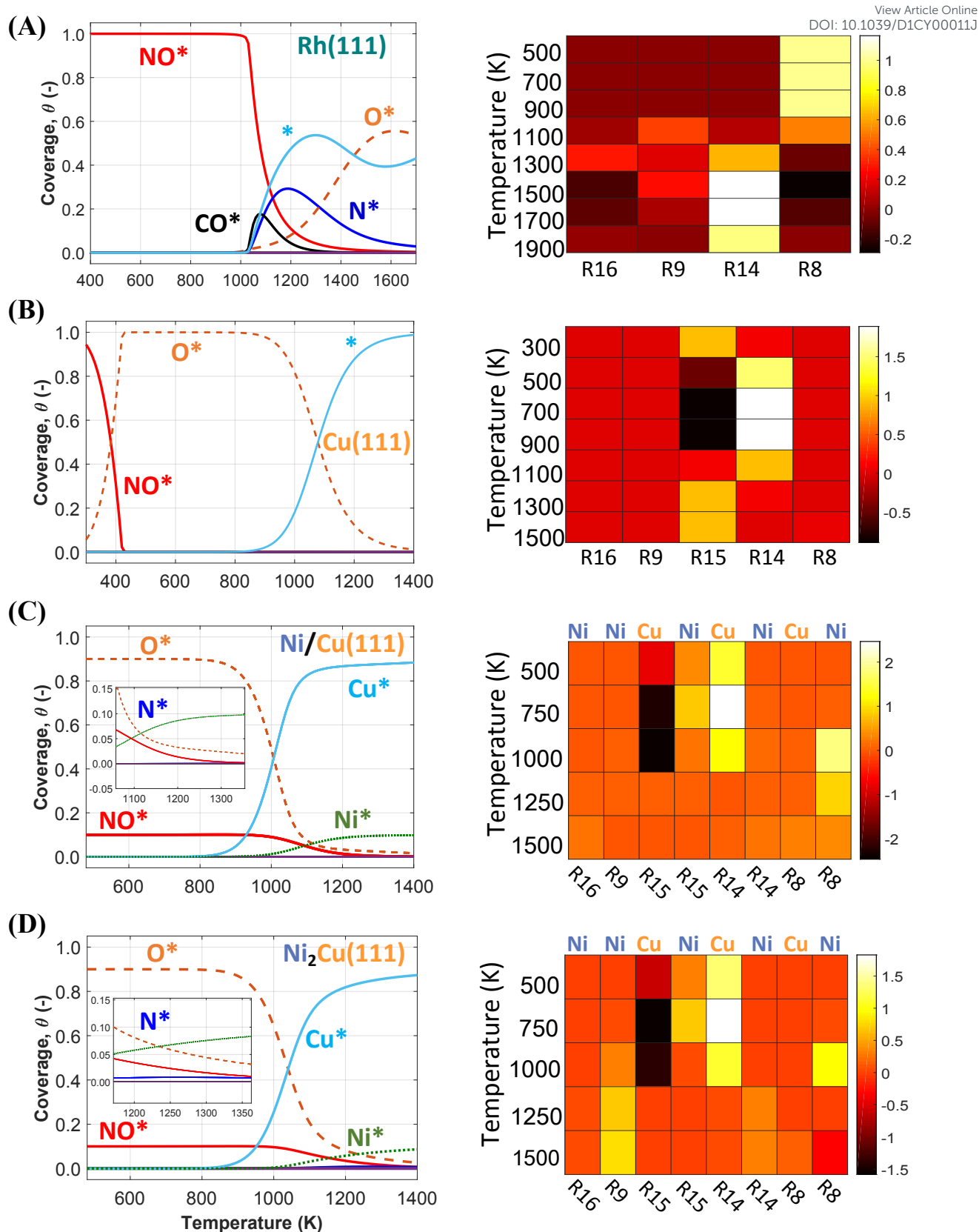


Figure 5. Total coverage (eq (4)) profiles and DRC coefficients (X_{RC}) for the NO + CO reaction steps for (A) Rh(111); (B) Cu(111); (C) Ni/Cu(111) SAA; and (D) Ni₂Cu(111). X_{RC} values are presented at various temperatures by means of heatmaps; the site whereon the reaction occurs is shown on the top of the heatmaps for the bimetallic surfaces.



Figure 6 displays the activity plots for the studied surfaces, where the catalytic rate is provided by the computed turnover frequency (TOF) at various temperatures. The observed trend for Rh(111) (Figure 6 (A)) can be rationalised based on the corresponding coverage plot (Figure 5 (A)). As seen in Figure 6 (A), the activity of Rh(111) is low below 950 K owing to the high NO* coverage, which hinders the direct NO* dissociation (Figure 5 (A)). On the contrary, for $T > 950$ K there is an increase in the catalytic activity. Initially the rate of N₂O production is greater than that of N₂, and only at $T > 1200$ K the two production rates become equal (Figure 6 (A)).

Similarly to Rh(111), the catalytic activity of Cu(111) can be explained from the coverage profile plot in Figure 5 (B). For this surface, low (i.e. 300 K – 500 K) and high (i.e. 500 K – 1400 K) temperatures can be discussed separately. Between 300 K and 420 K, we observe that the catalytic activity increases steadily (see Figure S11 in the Supporting Information), and the surface transitions from a NO*–rich phase to an O*–rich phase. As discussed earlier, this transition is associated with the dimerization reaction (R15 in Table 2), which consumes NO*, releases N₂O and yields O*. At ca. 420 K, there is a sharp reduction in the catalytic activity (Figure S11), and this is the result of the poisoning of Cu(111) by O* species. The surface remains in the poisoned state for temperatures up to ca. 700 K, where the removal of O* species happens efficiently and the dimerization reaction begins to take place again at considerable rates (see Figure 6 (B) and the heatmap in Figure 5 (B)). Finally, for $T > 1000$ K there is a decrease in the catalytic activity (Figure 6 (B)) because under these conditions, the gaseous state of the reactants is preferred over adsorption on the catalytic surface. Throughout the investigated temperature range, the production rate of N₂O is far greater than the production rate of N₂, and this is attributed to the inability of Cu(111) to directly dissociate NO* as well as to the weak binding of the η^1 N₂O* produced by the dimerization reaction.

On the other hand, enhanced catalytic activity can be achieved when Ni* species are present in Cu (111) (Figure 6 (C) and (D)). Remarkably, the production rate of N₂ is considerably larger on



Ni/Cu(111) SAA than on Cu(111) and even more so on Ni₂Cu(111), where the N₂ and N₂O production rates become equal beyond 1000 K.

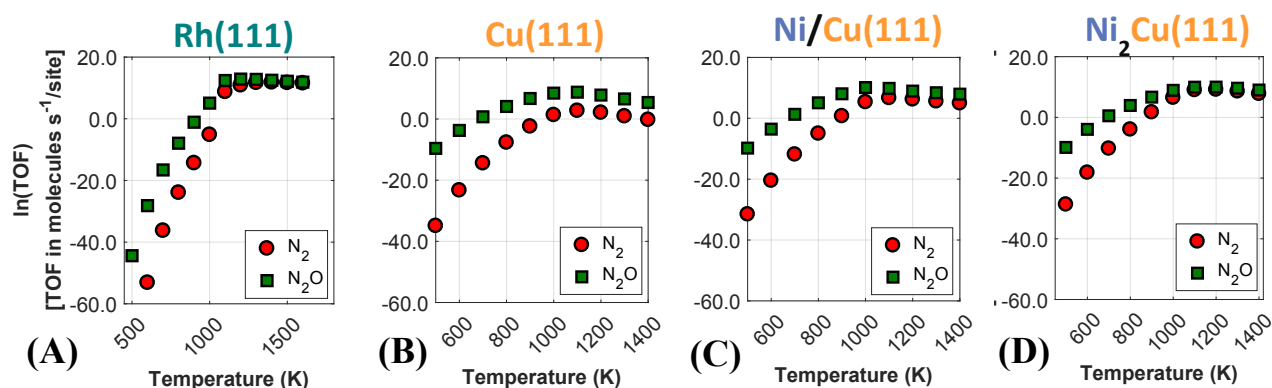


Figure 6. Rates of production of nitrogen-containing products for (A) Rh(111); (B) Cu(111); (C) Ni/Cu(111) SAA; and (D) Ni₂Cu(111).

Given the importance of S_{N_2}/S_{N_2O} , this section concludes with an investigation on this metric,

followed by suggestions for further improvements in this regard. Regarding Rh(111), our microkinetic model predicts that the main nitrogen-containing product from Rh(111) at $T < 1000$ K is N₂O, whilst the production of N₂ exhibits a substantial increase beyond 1100 K (Figure 7 (A)). The latter temperature corresponds to the point where the surface sites are freed up (Figure 5 (A)), and the dissociation of NO* is enabled. Notably, this trend is qualitatively in line with the reactor experiments of Peden et al.¹² on Rh(111). The experiments showed that Rh(111) exhibits poor selectivity to N₂ for reaction temperatures up to 700 K; yet, the authors observed a sharp increase in S_{N_2}/S_{N_2O} at temperatures higher than that. One should expect that closer quantitative agreement can be achieved by accounting for coverage effects, which will tend to decrease the surface coverage at $T < 1000$ K (see Figure S4), thereby freeing up sites and shifting the profiles of Figure 5 to lower temperatures.

The same analysis for Cu(111) reveals that this surface is indeed susceptible to the formation of N₂O (Figure 7 (A)). We find that the main way of forming N₂O* (in $\eta 1$ structure) on Cu(111) is via the formation of the (NO)₂* intermediate followed by N–O activation (R15). This is in line with molecular beam/infrared spectroscopy studies on other Cu low-index surfaces.⁷⁷ The $\eta 1$ N₂O* can go



through one of the following paths: (1) desorb directly ($E_a = 0.21$ eV); (2) transform to η^2NiO/N_2O^* ($E_a = 0.06$ eV) and either desorb ($E_a = 0.20$ eV) or dissociate to $N_2^* + O^*$ ($E_a = 0.05$ eV); (3) transform to $\eta^2NbNt N_2O^*$ ($E_a = 0.56$ eV) and desorb spontaneously. Therefore, N_2O^* can easily undergo transformations over Cu(111), but in every new state there is a high probability for desorption, thereby explaining the poor N_2 selectivity of this surface.

Interestingly, the catalytic behaviour Ni/Cu(111) SAA and $Ni_2Cu(111)$ appears to be more similar to Rh(111), which is well established for the NO + CO reaction, than to Cu(111), which is the host metal (Figure 7 (A)). In more precise terms, it is observed that on each of the dilute alloy surfaces the selectivity to N_2 remains low at $T < 900$ K but increases sharply at higher temperatures similarly to Rh(111). S_{N_2/N_2O} for both Ni/Cu(111) SAA and $Ni_2Cu(111)$ exhibits an interesting behaviour by which it first increases for $T > 900$ K and then decreases at 1200 K.

To shed light on this behaviour, we have carried out additional microkinetic simulations for $Ni_2Cu(111)$ where the activation barrier of one of the following events on Ni^* is assigned with a very large value (e.g. 2.5 eV): (1) NO^* direct dissociation (R8); (2) N_2^* formation (R16); (3) NO^* dimerization (R15); and (4) $\eta^2NbNt N_2O^*$ formation (R9). In doing so, we record how the selectivity peak responds to the obstruction of the aforementioned events (see section 9 in the Supporting Information). We determine that the selectivity spike in the two bimetallic surfaces is associated with the direct dissociation of NO^* and the formation of $\eta^2NbNt N_2O^*$, which could subsequently decompose to $N_2^* + O^*$ (see section 9 in the Supporting Information). Therefore, it is the ability of Ni/Cu alloys to form and process $\eta^2NbNt N_2O^*$ that gives rise to the selectivity peak in Figure 7 (A). The selectivity to N_2 enters a downturn because at $T > 1200$ K, there is a rise in the N_2O^* desorption rate. On the other hand, the formation of N_2 on Rh(111) is solely relying on the direct dissociation of NO^* and such a selectivity spike is not observed (Figure 7 (A)).



Accordingly, the higher intensity of the N₂ selectivity peak on Ni₂Cu(111) than on Ni/Cu(111)

SAA can be explained by: (1) the higher concentration of N* species on Ni₂Cu(111) owing to its better ability to dissociate NO* as compared to Ni/Cu(111) SAA (see Table 2 and Figure 5 (D)); (2) the generally stronger interaction between N₂O* and Ni₂Cu(111) than that between N₂O* and Ni/Cu(111) SAA (Table 2), noting that strong interaction will favour the decomposition of N₂O* over its desorption.

Moreover, we explore the effect of the N₂O* binding strength on the height of the selectivity peak on Ni₂Cu(111) by performing a sensitivity analysis with respect to $E_{ads}(N_2O)$ – (Figure 7 (B)). Remarkably, the adsorption energy of N₂O* appears to have a great impact upon the N₂ selectivity at 1100 K – 1200 K (Figure 7 (B)). For example, shifting the adsorption energy of all N₂O* adsorption structures to more negative values by 0.15 eV and 0.30 eV (i.e. stronger binding) results to an increase in the maximum of the peak by 0.31 (from 0.33 to 0.67) and 0.52 (from 0.33 to 0.85), respectively. We conjecture that binding strengths of this magnitude may be provided by sites on more open low-index surfaces (e.g. (100) and (110)) but also on stepped surfaces, and if this is true, the presence of such sites will contribute dramatically to the N₂ selectivity at low temperatures. Therefore, this result underscores the potential of well-engineered dilute Ni/Cu alloys for the NO + CO reaction and creates motivation for further investigations.



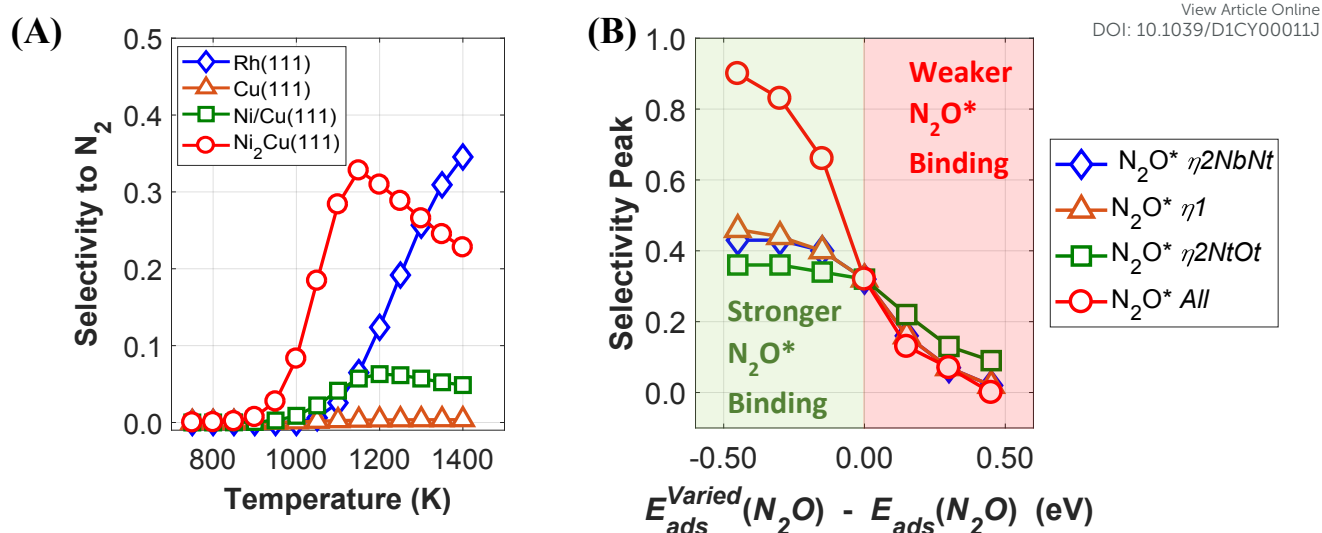


Figure 7. (A) Selectivity to N_2 for Cu(111), Rh(111) and the Ni/Cu alloys. (B) Maximum of the N_2 selectivity peak at various N_2O^* adsorption energies. Values on the right correspond to smaller N_2O^* binding strength on Ni^* than the DFT-computed (red shade); Values on the left correspond to larger N_2O^* binding strength on Ni^* than the DFT-computed (green shade). In the simulations of panel (B) only the desorption energy of N_2O^* was varied, whilst all the other kinetic barriers were kept fixed at their DFT-computed values.

Finally, given the importance of $E_{ads}(N_2O)$ we have computed the binding energy of N_2O^* using other vdW functionals, including optPBE–vdW, BEEF–vdW,⁹⁵ and the Tkatchenko–Scheffler method (DFT–TS) – (see Table S4 in the Supporting Information). The latter method is similar to the DFT–D2 method of Grimme,⁹⁶ with the difference that the dispersion coefficients and the damping function in the dispersion correction are dependent on the charge density.⁹⁷ These additional calculations highlight that significant variations in the predicted $E_{ads}(N_2O)$ should be expected when treating vdW interactions based on different approaches,⁹⁸ thereby influencing the predictions of ab initio microkinetic and kinetic Monte Carlo models (see section 11 in the Supporting Information).

4. Concluding remarks

By means of DFT calculations, we performed a thorough investigation of the formation and decomposition of N_2O^* over Rh(111), Cu(111), a Ni/Cu(111) SAA surface and a $Ni_2Cu(111)$ surface, where Ni atoms form dimer clusters. The DFT–derived energetics, in conjunction with results from our previous work,⁴ were then used to parameterise a microkinetic model for the NO + CO reaction.



Our DFT calculations showed that the presence of a small amount of Ni over Cu(111) strengthens significantly the interaction between N_2O^* and the catalyst surface. This enhanced interaction is desirable because it prevents the desorption of N_2O^* , thereby benefiting the selectivity to N_2 during the $NO + CO$ reaction. Regarding the decomposition of N_2O^* , we explored three competing reaction paths. In the first pathway the decomposition products (i.e. $NO^* + O^*$ and $N_2^* + O^*$) are connected through the $\eta 1$ adsorption structure of N_2O^* . In the second, the same products are connected through another N_2O^* adsorption structure (i.e. $\eta 2-(N_t\{fcc\}, O\{top\})$), and the third involves the formation of an $(NO)_2^*$ intermediate. These paths exhibit comparable energetics and therefore merit consideration when modelling the kinetics of the $NO + CO$ reaction. We also demonstrated that the selectivity of the Ni/Cu dilute alloy surfaces can be manipulated by tuning the size of the Ni cluster; generally, the formation of NO^* and atomic nitrogen is kinetically favoured over “large clusters” (e.g. trimers), whereas small clusters (i.e. dimers) and single atoms promote the dissociation of N_2O^* to N_2^* and atomic oxygen.

Finally, the performance of the Ni/Cu dilute alloy surfaces was assessed by means of microkinetic simulations for the $NO + CO$ reaction. Our studies highlighted the potential of $Ni_2Cu(111)$, which showed considerably improved catalytic performance as compared to $Cu(111)$ and comparable performance to the best transition metal for the reduction of NO (i.e. $Rh(111)$). Future work could focus on the effect of adsorbate–adsorbate interactions on the reaction kinetics of the $NO + CO$ reaction,^{99–101} and explore the behaviour of other facets of the Ni_2Cu catalyst in an effort to quantify potential structure–sensitivity effects.

Conflicts of interest

There are no conflicts of interest to declare

Acknowledgements

K. G. P. is funded by the Department of Chemical Engineering at University College London. The authors acknowledge the use of the UCL High Performance Computing Facilities Kathleen@UCL in



the completion of the simulations of this work. We are also grateful to the U.K. Materials and Molecular Modelling Hub, which is partially funded by EPSRC (EP/P020194/1), for computational resources (HPC facility Thomas). K. G. P. thanks Sai Yadavalli for fruitful discussions on the performance of DFT exchange and correlation functionals.

References

- 1 V. P. Zhdanov and B. Kasemo, *Surf. Sci. Rep.*, 1997, **29**, 31–33.
- 2 W. T. Wallace, Y. Cai, M. S. Chen and D. W. Goodman, *J. Phys. Chem. B*, 2006, **110**, 6245–6249.
- 3 D. Loffreda, D. Simon and P. Sautet, *J. Catal.*, 2003, **213**, 211–225.
- 4 K. G. Papanikolaou and M. Stamatakis, *Catal. Sci. Technol.*, 2020, **10**, 5815–5828.
- 5 H. J. Borg, J. F. C. J. M. Reijerse, R. A. Van Santen and J. W. Niemantsverdriet, *J. Chem. Phys.*, 1994, **101**, 10052–10063.
- 6 D. N. Belton, C. L. Dimaggio, S. J. Schmieg and K. Y. S. Ng, *J. Catal.*, 1995, **157**, 559–568.
- 7 K. C. Taylor, *Catal. Rev.*, 1993, **35**, 457–481.
- 8 F. Zaera and C. S. Gopinath, *Phys. Chem. Chem. Phys.*, 2003, **5**, 646–654.
- 9 C. S. Gopinath and F. Zaera, *J. Catal.*, 2001, **200**, 270–287.
- 10 C. H. F. Peden, D. W. Goodman, D. S. Blair, P. J. Berlowitz, G. B. Fisher and S. H. Oh, *J. Phys. Chem.*, 1988, **92**, 1563–1567.
- 11 L. H. Dubois, P. K. Hansma and G. A. Somorjai, *J. Catal.*, 1980, **65**, 318–327.
- 12 C. H. F. Peden, D. N. Belton and S. J. Schmieg, *J. Catal.*, 1995, **155**, 204–218.
- 13 G. S. Herman, C. H. F. Peden, S. J. Schmieg and D. N. Belton, *Catal. Letters*, 1999, **62**, 131–138.
- 14 H. Permana, K. Y. Simon Ng, C. H. F. Peden, S. J. Schmieg, D. K. Lambert and D. N. Belton, *Catal. Letters*, 1997, **47**, 5–15.
- 15 L. Tan, L. Huang, Y. Liu and Q. Wang, *Appl. Surf. Sci.*, 2018, **444**, 276–286.
- 16 A. Ishikawa and Y. Tateyama, *J. Phys. Chem. C*, 2018, **122**, 17378–17383.
- 17 J. Liu, L. Tan, L. Huang, Q. Wang and Y. Liu, *Langmuir*, 2020, **36**, 3127–3140.
- 18 V. P. Zhdanov and B. Kasemo, *Catal. Letters*, 1996, **40**, 197–202.
- 19 J. Cortés and E. Valencia, *J. Phys. Chem. B*, 2006, **110**, 7887–7897.
- 20 C. Y. Kang, M. Taniguchi, M. Uenishi and H. Tanaka, *Chem. Lett.*, 2012, **41**, 822–824.
- 21 H. Asakura, T. Onuki, S. Hosokawa, N. Takagi, S. Sakaki, K. Teramura and T. Tanaka, *Phys. Chem. Chem. Phys.*, 2019, **21**, 18816–18822.



- 22 K. Ueda, C. A. Ang, Y. Ito, J. Ohyama and A. Satsuma, *Catal. Sci. Technol.*, 2016, **6**, 5797–5800. Article Online
DOI: 10.1039/D1CY00011J
- 23 H. Yoshida, Y. Okabe, N. Yamashita, S. Hinokuma and M. Machida, *Catal. Today*, 2017, **281**, 590–595.
- 24 K. Koizumi, H. Yoshida, M. Boero, K. Tamai, S. Hosokawa, T. Tanaka, K. Nobusada and M. Machida, *Phys. Chem. Chem. Phys.*, 2018, **20**, 25592–25601.
- 25 H. Yoshida, N. Yamashita, S. Ijichi, Y. Okabe, S. Misumi, S. Hinokuma and M. Machida, *ACS Catal.*, 2015, **5**, 6738–6747.
- 26 T. Hirakawa, Y. Shimokawa, W. Tokuzumi, T. Sato, M. Tsushida, H. Yoshida, J. Ohyama and M. Machida, *ACS Appl. Nano Mater.*, 2020, **3**, 9097–9107.
- 27 N. Takagi, K. Ishimura, H. Miura, T. Shishido, R. Fukuda, M. Ehara and S. Sakaki, *ACS Omega*, 2019, **4**, 2596–2609.
- 28 H. Yoshida, Y. Kawakami, W. Tokuzumi, Y. Shimokawa, T. Hirakawa, J. Ohyama and M. Machida, *Bull. Chem. Soc. Jpn.*, 2020, **93**, 1050–1055.
- 29 C. B. Jones, I. Khurana, S. H. Krishna, A. J. Shih, W. N. Delgass, J. T. Miller, F. H. Ribeiro, W. F. Schneider and R. Gounder, *J. Catal.*, 2020, **389**, 140–149.
- 30 Y. Nishihata, J. Mizuki, T. Akao, H. Tanaka, M. Uenishi, M. Kimura, T. Okamoto and N. Hamada, *Nature*, 2002, **418**, 164–167.
- 31 S. Hosokawa, T. Shibano, H. Koga, M. Matsui, H. Asakura, K. Teramura, M. Okumura and T. Tanaka, *ChemCatChem*, 2020, **12**, 4276–4280.
- 32 L. Zhang, I. A. W. Filot, Y.-Q. Su, J.-X. Liu and E. J. M. Hensen, *J. Catal.*, 2018, **363**, 154–163.
- 33 F. Xing, J. Jeon, T. Toyao, K. Shimizu and S. Furukawa, *Chem. Sci.*, 2019, **10**, 8292–8298.
- 34 R. Réocreux, P. L. Kress, R. T. Hannagan, V. Çınar, M. Stamatakis and E. C. H. Sykes, *J. Phys. Chem. Lett.*, 2020, **11**, 8751–8757.
- 35 S. Kandoi, A. A. Gokhale, L. C. Grabow, J. A. Dumesic and M. Mavrikakis, *Catal. Letters*, 2004, **93**, 93–100.
- 36 F. Zaera and C. S. Gopinath, *Chem. Phys. Lett.*, 2000, **332**, 209–214.
- 37 W. B. Tolman, *Angew. Chemie - Int. Ed.*, 2010, **49**, 1018–1024.
- 38 H. Tian, R. Xu, J. G. Canadell, R. L. Thompson, W. Winiwarter, P. Suntharalingam, E. A. Davidson, P. Ciais, R. B. Jackson, G. Janssens-Maenhout, M. J. Prather, P. Regnier, N. Pan, S. Pan, G. P. Peters, H. Shi, F. N. Tubiello, S. Zaehle, F. Zhou, A. Arneeth, G. Battaglia, S. Berthet, L. Bopp, A. F. Bouwman, E. T. Buitenhuis, J. Chang, M. P. Chipperfield, S. R. S. Dangal, E. Dlugokencky, J. W. Elkins, B. D. Eyre, B. Fu, B. Hall, A. Ito, F. Joos, P. B. Krummel, A. Landolfi, G. G. Laruelle, R. Lauerwald, W. Li, S. Lienert, T. Maavara, M. MacLeod, D. B. Millet, S. Olin, P. K. Patra, R. G. Prinn, P. A. Raymond, D. J. Ruiz, G. R. van der Werf, N. Vuichard, J. Wang, R. F. Weiss, K. C. Wells, C. Wilson, J. Yang and Y. Yao, *Nature*, 2020, **586**, 248–256.
- 39 G. Kresse and J. Furthmüller, *Comput. Mater. Sci.*, 1996, **6**, 15–50.
- 40 G. Kresse and J. Hafner, *Phys. Rev. B*, 1993, **47**, 558–561.



- 41 M. Dion, H. Rydberg, E. Schröder, D. C. Langreth and B. I. Lundqvist, *Phys. Rev. Lett.*, 2004, **92**, 246401. View Article Online
DOI: 10.1039/B1CV00011J
- 42 J. Klimeš, D. R. Bowler and A. Michaelides, *J. Phys. Condens. Matter*, 2010, **22**, 022201.
- 43 A. Shiotari, S. Hatta, H. Okuyama and T. Aruga, *J. Chem. Phys.*, 2014, **141**, 134705.
- 44 J. Klimeš, D. R. Bowler and A. Michaelides, *Phys. Rev. B*, 2011, **83**, 195131.
- 45 P. E. Blöchl, *Phys. Rev. B*, 1994, **50**, 17953–17979.
- 46 P. Haas, F. Tran and P. Blaha, *Phys. Rev. B*, 2009, **79**, 085104.
- 47 J. D. Pack and H. J. Monkhorst, *Phys. Rev. B*, 1977, **16**, 1748–1749.
- 48 G. Henkelman and H. Jónsson, *J. Chem. Phys.*, 1999, **111**, 7010–7022.
- 49 K. W. Kolasinski, in *Surface Science*, John Wiley & Sons, Ltd, Chichester, UK, 2012, pp. 51–114.
- 50 W. F. K. Wynne-Jones and H. Eyring, *J. Chem. Phys.*, 1935, **3**, 492–502.
- 51 C. T. Campbell, *ACS Catal.*, 2017, **7**, 2770–2779.
- 52 C. Stegelmann, A. Andreasen and C. T. Campbell, *J. Am. Chem. Soc.*, 2009, **131**, 8077–8082.
- 53 Y. Li and M. Bowker, *Surf. Sci.*, 1996, **348**, 67–76.
- 54 A. Bogicevic and K. C. Hass, *Surf. Sci.*, 2002, **506**, L237–L242.
- 55 V. G. Komvokis, M. Marti, A. Delimitis, I. A. Vasalos and K. S. Triantafyllidis, *Appl. Catal. B Environ.*, 2011, **103**, 62–71.
- 56 A. Kokalj, I. Kobal and T. Matsushima, *J. Phys. Chem. B*, 2003, **107**, 2741–2747.
- 57 S. Y. Wu, C. H. Su, J. G. Chang, H. T. Chen, C. H. Hou and H. L. Chen, *Comput. Mater. Sci.*, 2011, **50**, 3311–3314.
- 58 H. Orita and N. Itoh, *Surf. Sci.*, 2004, **550**, 166–176.
- 59 R. Burch, S. T. Daniells and P. Hu, *J. Chem. Phys.*, 2004, **121**, 2737.
- 60 X. Wei, X. F. Yang, A. Q. Wang, L. Li, X. Y. Liu, T. Zhang, C. Y. Mou and J. Li, *J. Phys. Chem. C*, 2012, **116**, 6222–6232.
- 61 K. Kim, S. Baek, J. J. Kim and J. W. Han, *Appl. Surf. Sci.*, 2020, **510**, 145349.
- 62 J.-F. Paul, J. Pérez-Ramírez, F. Ample and J. M. Ricart, *J. Phys. Chem. B*, 2004, **108**, 17921–17927.
- 63 J. L. Teffo and A. Chédin, *J. Mol. Spectrosc.*, 1989, **135**, 389–409.
- 64 M. D. Marcinkowski, M. T. Darby, J. Liu, J. M. Wimble, F. R. Lucci, S. Lee, A. Michaelides, M. Flytzani-Stephanopoulos, M. Stamatakis and E. C. H. Sykes, *Nat. Chem.*, 2018, **10**, 325–332.
- 65 M. B. Boucher, B. Zugic, G. Cladaras, J. Kammert, M. D. Marcinkowski, T. J. Lawton, E. C. H. Sykes and M. Flytzani-Stephanopoulos, *Phys. Chem. Chem. Phys.*, 2013, **15**, 12187–12196.
- 66 R. T. Hannagan, G. Giannakakis, M. Flytzani-Stephanopoulos and E. C. H. Sykes, *Chem.*



- Rev., 2020, *acs.chemrev*.0c00078.
- 67 M. T. Darby, M. Stamatakis, A. Michaelides and E. C. H. Sykes, *J. Phys. Chem. Lett.*, 2018, **9**, 5636–5646.
- 68 D. A. Patel, R. T. Hannagan, P. L. Kress, A. C. Schilling, V. Çınar and E. C. H. Sykes, *J. Phys. Chem. C*, 2019, **123**, 28142–28147.
- 69 G. Giannakakis, M. Flytzani-Stephanopoulos and E. C. H. Sykes, *Acc. Chem. Res.*, 2019, **52**, 237–247.
- 70 G. Kyriakou, M. B. Boucher, A. D. Jewell, E. a Lewis, T. J. Lawton, A. E. Baber, H. L. Tierney, M. Flytzani-Stephanopoulos and E. C. H. Sykes, *Science (80-.)*, 2012, **335**, 1209–1212.
- 71 J. Liu, F. R. Lucci, M. Yang, S. Lee, M. D. Marcinkowski, A. J. Therrien, C. T. Williams, E. C. H. Sykes and M. Flytzani-Stephanopoulos, *J. Am. Chem. Soc.*, 2016, **138**, 6396–6399.
- 72 K. G. Papanikolaou, M. T. Darby and M. Stamatakis, *ACS Catal.*, 2020, **10**, 1224–1236.
- 73 K. G. Papanikolaou, M. T. Darby and M. Stamatakis, *J. Phys. Chem. C*, 2019, **123**, 9128–9138.
- 74 M. T. Darby, E. C. H. Sykes, A. Michaelides and M. Stamatakis, *Top. Catal.*, 2018, **61**, 428–438.
- 75 M. Ouyang, K. G. Papanikolaou, A. Boubnov, A. S. Hoffman, G. Giannakakis, S. R. Bare, M. Stamatakis, M. Flytzani-Stephanopoulos and E. C. H. Sykes, *Nat. Commun. Accept.*, , DOI:10.1038/s41467-021-21555-z.
- 76 H. Thirumalai and J. R. Kitchin, *Top. Catal.*, 2018, **61**, 462–474.
- 77 W. A. Brown, R. K. Sharma, D. A. King and S. Haq, *J. Phys. Chem.*, 1996, **100**, 12559–12568.
- 78 Y. Wang, D. Zhang, Z. Yu and C. Liu, *J. Phys. Chem. C*, 2010, **114**, 2711–2716.
- 79 Z. P. Liu, S. J. Jenkins and D. A. King, *J. Am. Chem. Soc.*, 2004, **126**, 7336–7340.
- 80 T. N. Pham, Y. Hamamoto, K. Inagaki, D. N. Son, I. Hamada and Y. Morikawa, *J. Phys. Chem. C*, 2020, **124**, 2968–2977.
- 81 I. Nakai, H. Kondoh, T. Shimada, R. Yokota, T. Katayama, T. Ohta and N. Kosugi, *J. Chem. Phys.*, 2007, **127**, 024701.
- 82 K. G. Papanikolaou, M. T. Darby and M. Stamatakis, *J. Chem. Phys.*, 2018, **149**, 184701.
- 83 M. Stamatakis, *J. Phys. Condens. Matter*, 2015, **27**, 013001.
- 84 K. G. Papanikolaou and M. Stamatakis, in *Computational Modelling of Nanomaterials*, 2020, pp. 95–125.
- 85 M. Stamatakis and S. Piccinin, *ACS Catal.*, 2016, **6**, 2105–2111.
- 86 J. K. Nørskov, F. Studt, F. Abild-Pedersen and T. Bligaard, in *Fundamental Concepts in Heterogeneous Catalysis*, John Wiley & Sons, Inc, Hoboken, NJ, USA, 2014, pp. 68–84.
- 87 L. C. Grabow and M. Mavrikakis, *ACS Catal.*, 2011, **1**, 365–384.



- 88 S. Li, S. Singh, J. A. Dumesic and M. Mavrikakis, *Catal. Sci. Technol.*, 2019, **9**, 2836–2848. View Article Online
DOI: 10.1039/C9CY00011J
- 89 S. Bhandari, S. Rangarajan and M. Mavrikakis, *Acc. Chem. Res.*, 2020, **53**, 1893–1904.
- 90 Y. Xu and M. Mavrikakis, *Surf. Sci.*, 2001, **494**, 131–144.
- 91 A. C. Lausche, A. J. Medford, T. S. Khan, Y. Xu, T. Bligaard, F. Abild-Pedersen, J. K. Nørskov and F. Studt, *J. Catal.*, 2013, **307**, 275–282.
- 92 J. Schumann, A. J. Medford, J. S. Yoo, Z. J. Zhao, P. Bothra, A. Cao, F. Studt, F. Abild-Pedersen and J. K. Nørskov, *ACS Catal.*, 2018, **8**, 3447–3453.
- 93 S. González, C. Sousa and F. Illas, *J. Catal.*, 2006, **239**, 431–440.
- 94 M. Mavrikakis, J. Rempel, J. Greeley, L. B. Hansen and J. K. Nørskov, *J. Chem. Phys.*, 2002, **117**, 6737–6744.
- 95 J. Wellendorff, K. T. Lundgaard, A. Møgelhøj, V. Petzold, D. D. Landis, J. K. Nørskov, T. Bligaard and K. W. Jacobsen, *Phys. Rev. B*, 2012, **85**, 235149.
- 96 S. Grimme, *J. Comput. Chem.*, 2006, **27**, 1787–1799.
- 97 A. Tkatchenko and M. Scheffler, *Phys. Rev. Lett.*, 2009, **102**, 6–9.
- 98 S. Gautier, S. N. Steinmann, C. Michel, P. Fleurat-Lessard and P. Sautet, *Phys. Chem. Chem. Phys.*, 2015, **17**, 28921–28930.
- 99 R. B. Getman, Y. Xu and W. F. Schneider, *J. Phys. Chem. C*, 2008, 9559–9572.
- 100 S. Matera, W. F. Schneider, A. Heyden and A. Savara, *ACS Catal.*, 2019, **9**, 6624–6647.
- 101 D. J. Schmidt, W. Chen, C. Wolverton and W. F. Schneider, *J. Chem. Theory Comput.*, 2012, **8**, 264–273.



Supporting Information for

The Catalytic Decomposition of Nitrous Oxide and the NO

+ CO Reaction over Ni/Cu Dilute and Single Atom Alloy

Surfaces: First-principles Microkinetic Modelling

Konstantinos G. Papanikolaou and Michail Stamatakis*

Thomas Young Centre and Department of Chemical Engineering, University College London,

Roberts Building, Torrington Place, London WC1E 7JE, UK

1. Adsorption of N₂O on Rh(111), Cu(111), Ni/Cu(111) SAA and Ni₂Cu(111)

Figure S1 shows the six identified N₂O adsorption structures, and Table S1 summarises the computed adsorption energies and bond lengths.

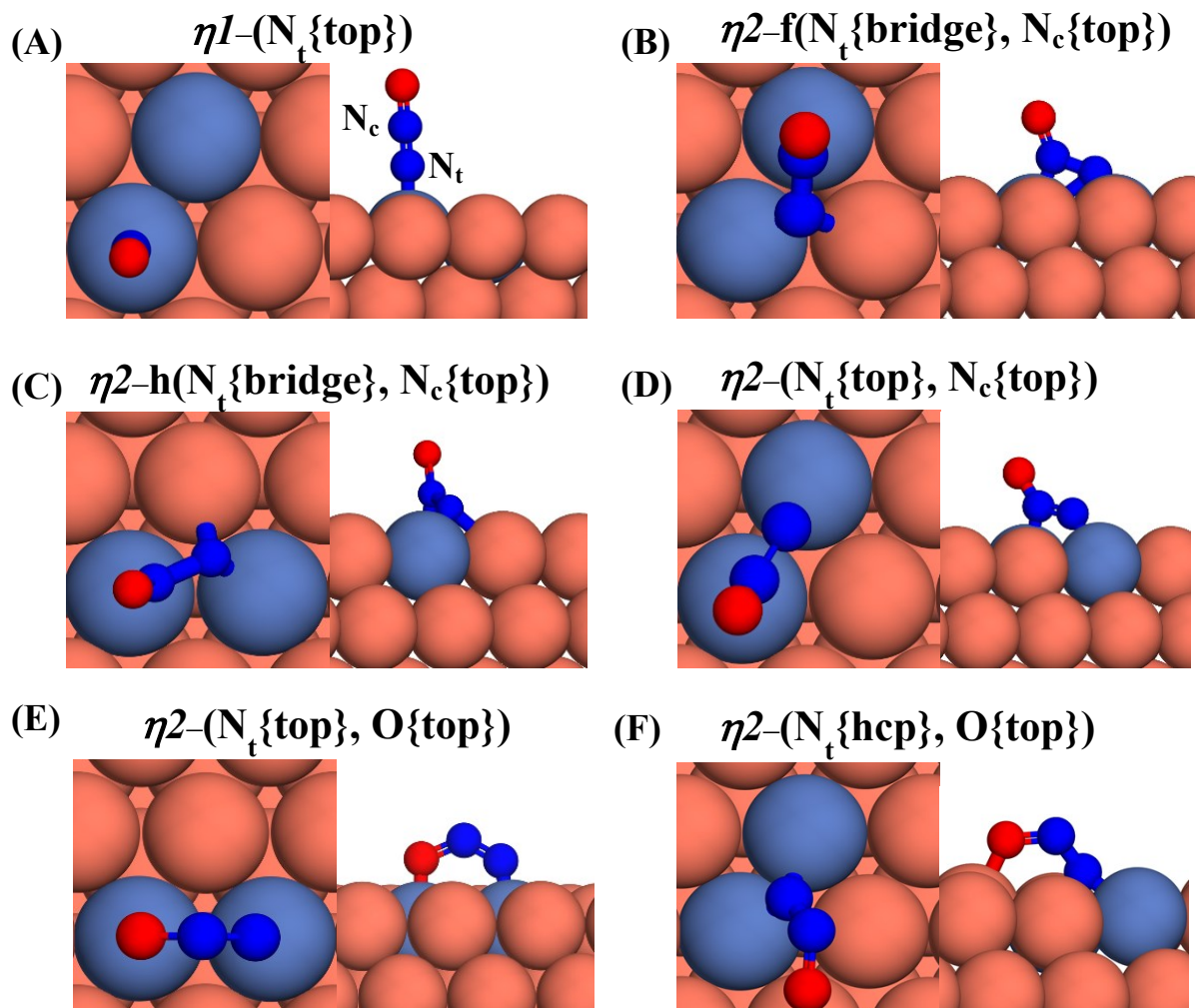


Figure S1. Top and side views of (A) $\eta 1-(N_t\{\text{top}\})$; (B) $\eta 2-f(N_t\{\text{bridge}\}, N_c\{\text{top}\})$; (C) $\eta 2-h(N_t\{\text{bridge}\}, N_c\{\text{top}\})$; (D) $\eta 2-(N_t\{\text{top}\}, N_c\{\text{top}\})$; (E) $\eta 2-(N_t\{\text{top}\}, O\{\text{top}\})$ and (F) $\eta 2-(N_t\{\text{hcp}\}, O\{\text{top}\})$ adsorption structure. On the side view of (a) we highlight the terminal (N_t) and central (N_c) nitrogen atoms. Ni, Cu, N and O atoms are shown in purple, orange, blue and red, respectively. The adsorption geometries are shown over Ni₂Cu(111), but they are representative for all surfaces

Table S1. Adsorption energies (in eV) and bond distances (in Å) for the different N₂O* adsorption geometries over the investigated surfaces. The adsorption energies and bond distances that correspond to the most stable adsorption structure(s) for each surface are shown in bold. A dash indicates either that the adsorption structure is not stable on the specific surface or that it is not a minimum on the potential energy surface (i.e. there was an imaginary frequency in the vibrational analysis). For comparison: $d_{N-N} = 1.14$ Å and $d_{N-O} = 1.20$ Å for gas N₂O.

Adsorption Structure	Property	Rh(111)	Cu(111)	Ni/Cu(111) SAA	Ni ₂ Cu(111)
$\eta 1-(N_t\{\text{top}\})$ (denoted as $\eta 1$)	$E_{ads}(N_2O)$	-0.71	-0.21	-0.70	-0.68
	d_{N-O}	1.20	1.20	1.20	1.21
	d_{N-N}	1.15	1.15	1.15	1.15
$\eta 2-f(N_t\{\text{bridge}\}, N_c\{\text{top}\})$ (denoted as $\eta 2NbNt$)	$E_{ads}(N_2O)$	-0.83	+0.15	-0.43	-0.74
	d_{N-O}	1.22	1.23	1.23	1.23
	d_{N-N}	1.35	1.29	1.29	1.31
$\eta 2-h(N_t\{\text{bridge}\}, N_c\{\text{top}\})$	$E_{ads}(N_2O)$	-0.83	+0.15	-0.41	-0.73
	d_{N-O}	1.22	1.23	1.23	1.23
	d_{N-N}	1.36	1.29	1.28	1.30
$\eta 2-(N_t\{\text{top}\}, N_c\{\text{top}\})$	$E_{ads}(N_2O)$	-0.68	+0.27	–	-0.62
	d_{N-O}	1.25	1.23	–	1.24
	d_{N-N}	1.26	1.22	–	1.25
$\eta 2-(N_t\{\text{top}\}, O\{\text{top}\})$ (denoted as $\eta 2NiOt$)	$E_{ads}(N_2O)$	-0.72	-0.20	-0.53	-0.68
	d_{N-O}	1.33	1.28	1.30	1.32
	d_{N-N}	1.20	1.19	1.20	1.20
$\eta 2-(N_t\{\text{hcp}\}, O\{\text{top}\})$	$E_{ads}(N_2O)$	–	-0.25	-0.44	-0.73
	d_{N-O}	–	1.30	1.31	1.32
	d_{N-N}	–	1.27	1.25	1.27

2. Electronic structure analyses of N₂O adsorption modes

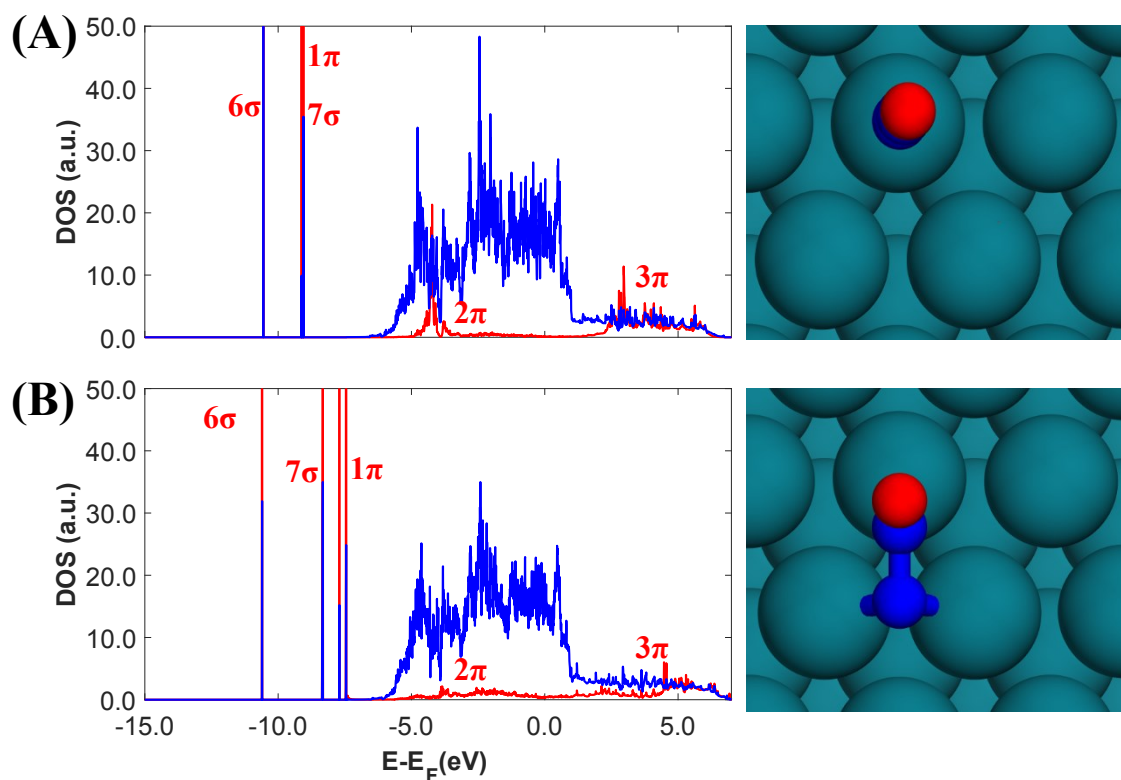


Figure S2. Projected density of states for (A) the η_1 -(N_t{top}); and (B) the η_2 -h(N_t{bridge}, N_c{top}) on Rh(111). The red line is the N₂O* contribution and the blue line is the metal contribution (only Rh surface atoms). The relaxed adsorption structures are shown on the right of each panel. Rh, O and N atoms are shown in dark green, red and blue.

3. Reaction path for N₂O formation and decomposition

Figure S3 shows the reaction path for the decomposition of N₂O to either NO* + N* or N₂* + O*. The energies presented are referenced to a non-interacting N₂O molecule in the gas-phase and a clean Rh(111) slab. For an accurate comparison of our results to the work of Paul et al.,¹ all the energies presented include the zero point energy (ZPE) correction, which can be introduced by calculating the energy of an adsorbed state as

$$E_{DFT,s} = E_{DFT}^{Slab+N_2O} - E_{DFT}^{Slab} - E_{DFT}^{N_2O(g)} + \hbar \left(\sum_{i=1}^9 \frac{\omega_i}{2} - \sum_{i=1}^3 \frac{\omega_{N_2O,i}}{2} \right), \quad (S1)$$

where $E_{DFT,s}$ is the energy of a state s ; $E_{DFT}^{Slab+N_2O}$, E_{DFT}^{Slab} and $E_{DFT}^{N_2O(g)}$ are the DFT energies for a Rh(111) slab whereon N₂O is adsorbed, clean Rh(111) slab and a gas-phase N₂O molecule; \hbar is the reduced Planck constant; $\omega_{N_2O,i}$ is the angular frequency of the i^{th} mode of gas-phase N₂O and ω_i is the angular frequency of the i^{th} mode of N₂O in an adsorbed state.

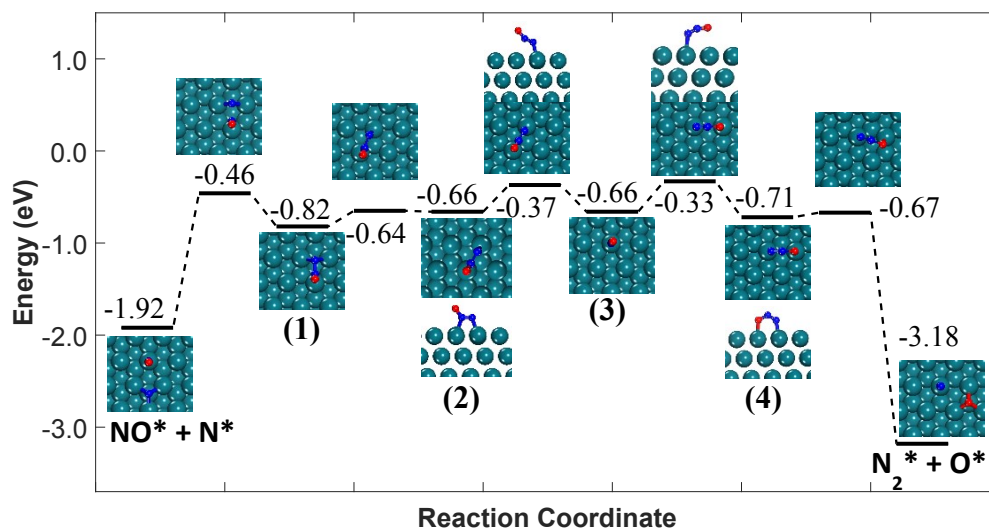


Figure S3. Reaction path for the decomposition of N₂O* either to NO* + N* or to N₂* + O*. The energy values are ZPE-corrected. The numbering of the adsorbed configurations of N₂O is as follows: (1) η^2 -f(N_i{bridge}, N_c{top}), (2) η^2 -(N_i{top}, N_c{top}), (3) η^1 -(N_i{top}) and (4) η^2 -(N_i{top}, O{top}). Rh, O and N atoms are shown in dark green, red and blue, respectively.

4. NO* – NO* repulsive interactions

To demonstrate the NO* – NO* repulsive interactions, we plot the average adsorption energy of NO* over Rh(111) for different NO* surface coverages. As seen, at increasing surface coverage the NO* binding strength diminishes (i.e. less exothermic adsorption).

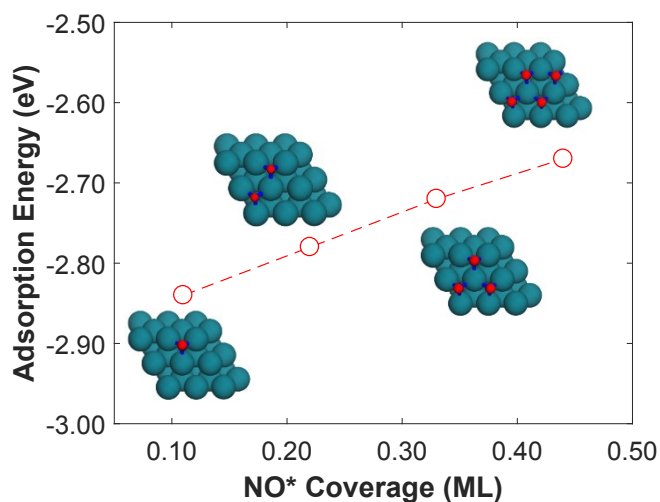


Figure S4. Average adsorption of NO* for various coverages. Rh, O and N atoms are shown in dark green, red and blue, respectively.

5. N₂O* formation via (NO)₂* on Ni₃Cu(111)

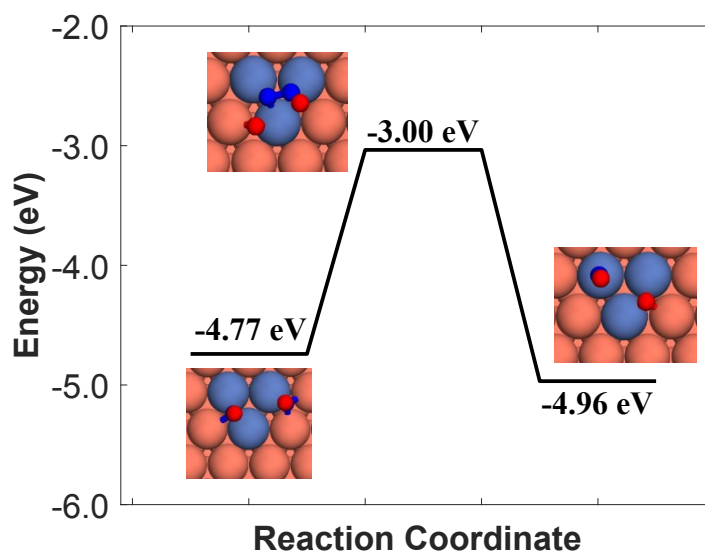


Figure S5. N₂O* formation via (NO)₂* on Ni₃Cu(111).

6. Side views of the states within the N_2O^* formation and decomposition reaction pathways

The following figures show the side view of the different states that are involved in the N_2O^* formation/decomposition pathways (see Figure 2, Figure 3 and Figure 4 in the main text). The images are for the $\text{Ni}_2\text{Cu}(111)$ surface, but in the vast majority of cases they are representative for all the Cu-based surfaces.

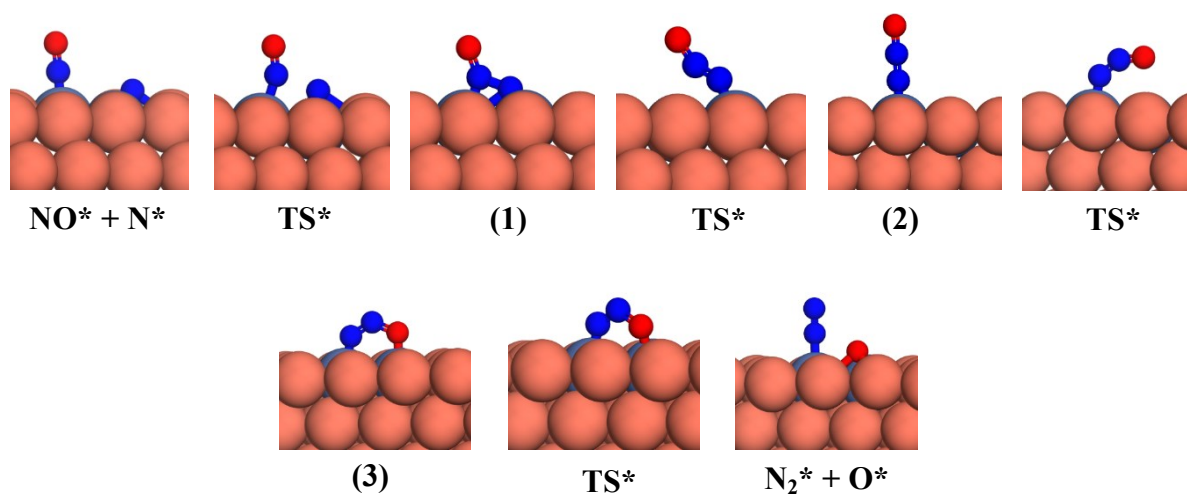


Figure S6. Side views of the states in Figure 2 (B) of the main text. Ni, Cu, O and N atoms are shown in purple, orange, red and blue, respectively.

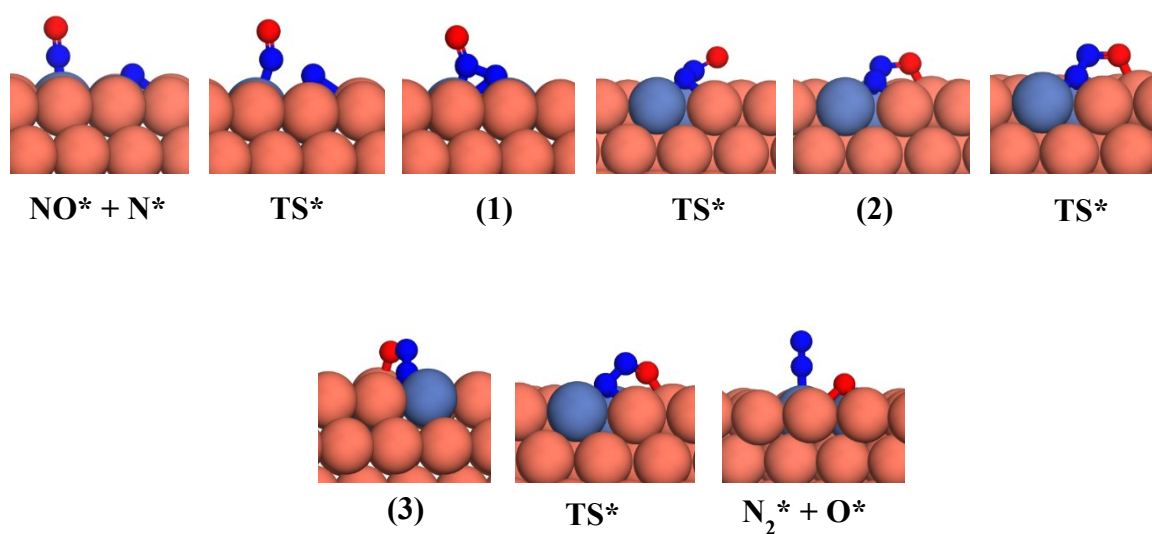


Figure S7. Side views of the states in Figure 3 (C) of the main text. Ni, Cu, O and N atoms are shown in purple, orange, red and blue, respectively.

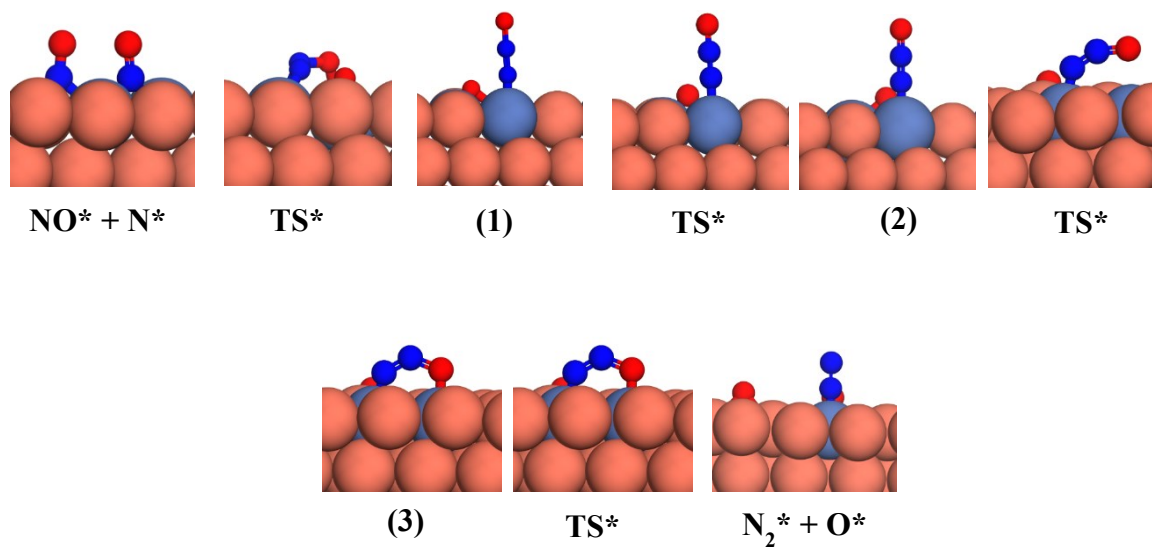


Figure S8. Side views of the states in Figure 4 (C) of the main text. Ni, Cu, O and N atoms are shown in purple, orange, red and blue, respectively.

7. O₂* association and NO₂* formation

Figure S9 shows the initial, transition and final states for the formation of O₂* from two O* adatoms. Also shown are the computed DFT energies for each structure.

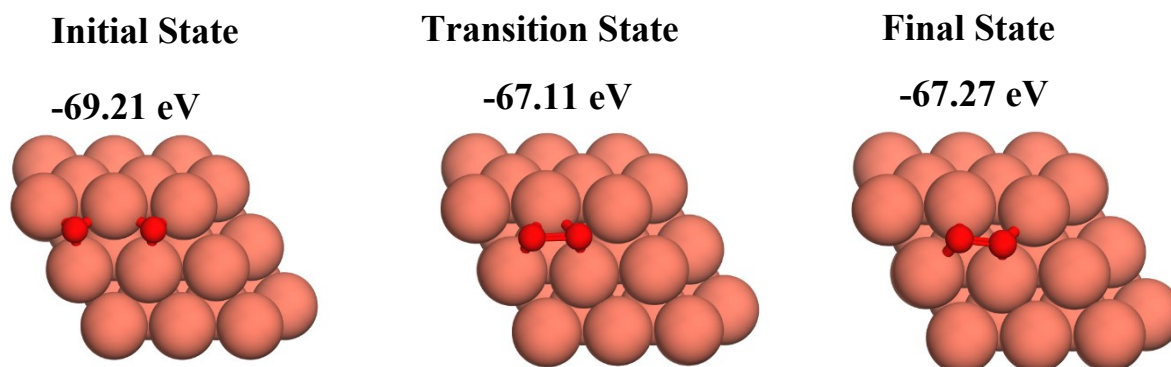


Figure S9. Top view of initial, transition and final states for the formation of O₂* on Cu(111). Cu and O atoms are shown in orange and red, respectively.

Regarding the NO₂* formation, we find that on Cu-based the forward barrier is always larger than 0.70 eV, while the reverse barrier (i.e. NO₂* dissociation) is always smaller than 0.30 eV. Our data indicates that the formation of NO₂* is neither kinetically nor thermodynamically favoured. The most stable final state for all the three surfaces is the so-called μ -N,O-nitrito adsorption mode, whose stability is experimentally confirmed on other coinage metal surfaces.² We also compute the adsorption energies of NO₂* in the μ -N,O-nitrito structure on the Cu-based surfaces (Table S2). The obtained values imply that even if NO₂* is formed on the surface its dissociation will be dramatically more favourable than its desorption, thereby corroborating our reaction mechanism, which does not take into account the formation of NO₂*.

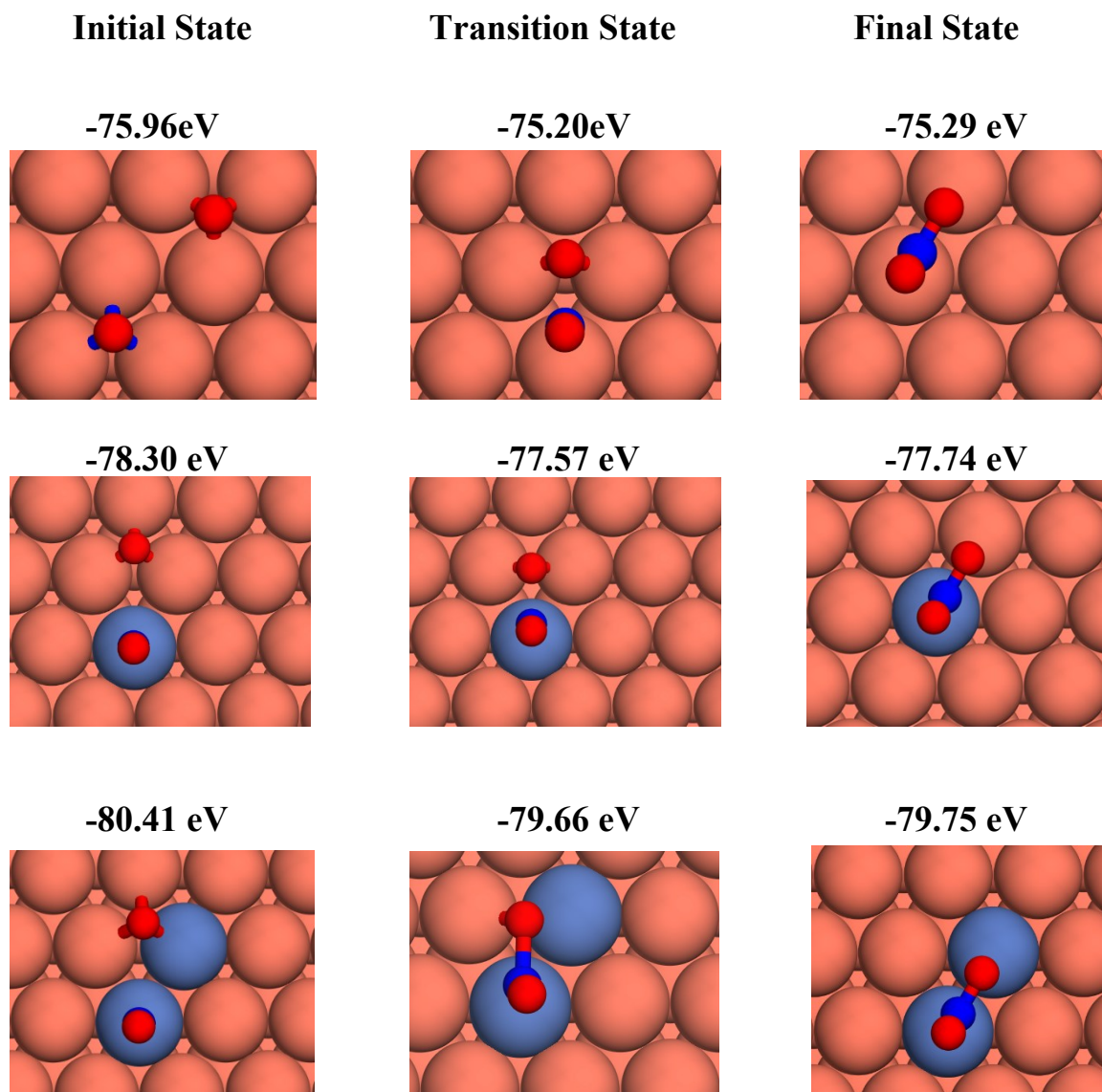


Figure S10. Top view of initial, transition and final states for the formation of NO_2^* on Cu(111), Ni/Cu(111) SAA and Ni_2Cu (111) surfaces. Ni, Cu, O and N atoms are shown in purple, orange, red and blue, respectively.

Table S2. Adsorption energies for NO₂* in μ -N,O-nitrito adsorption structure on Cu-based surfaces. Note that the gas-phase calculation for NO_{2(g)} was spin-polarised.

Surface	E_{ads}(NO₂)
Cu(111)	-1.70 eV
Ni/Cu(111) SAA	-2.10 eV
Ni₂Cu(111)	-2.30 eV

8. Activity plot for Cu(111) at “low temperatures”

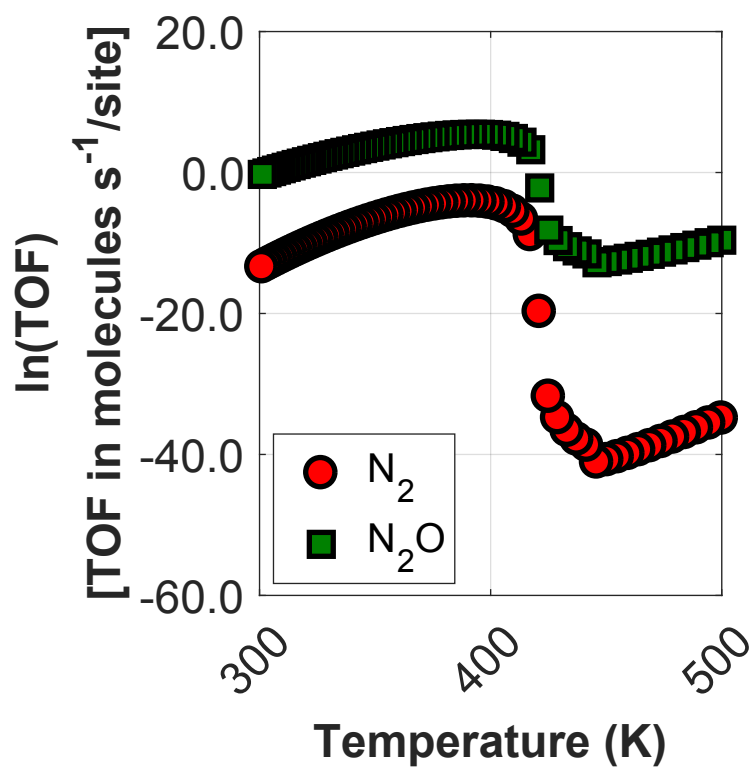


Figure S11. Activity of Cu(111) within the temperature range of 300 K – 500 K (Low-temperature range).

9. Explanation for the selectivity peak on Ni/Cu bimetallic alloys

Figure S12 (A) and (B) shows that the selectivity peak of Ni₂Cu(111) is unaffected by changes to the activation barrier to the formation of N₂* (R16 in Table 2 in the main text) and the dimerization reaction (R15 in Table 2 in the main text) on Ni*. On the contrary, the peak (which appears between 950 K and 1400 K) disappears upon increasing the activation barrier for the formation of N₂O* (R9 in Table 2 in the main text) and NO* dissociation (R8 in Table 2 in the main text) reactions on Ni*. Therefore, the selectivity spike for Ni/Cu SAA and Ni₂Cu in Figure 7 (A) is associated only with the latter two reactions.

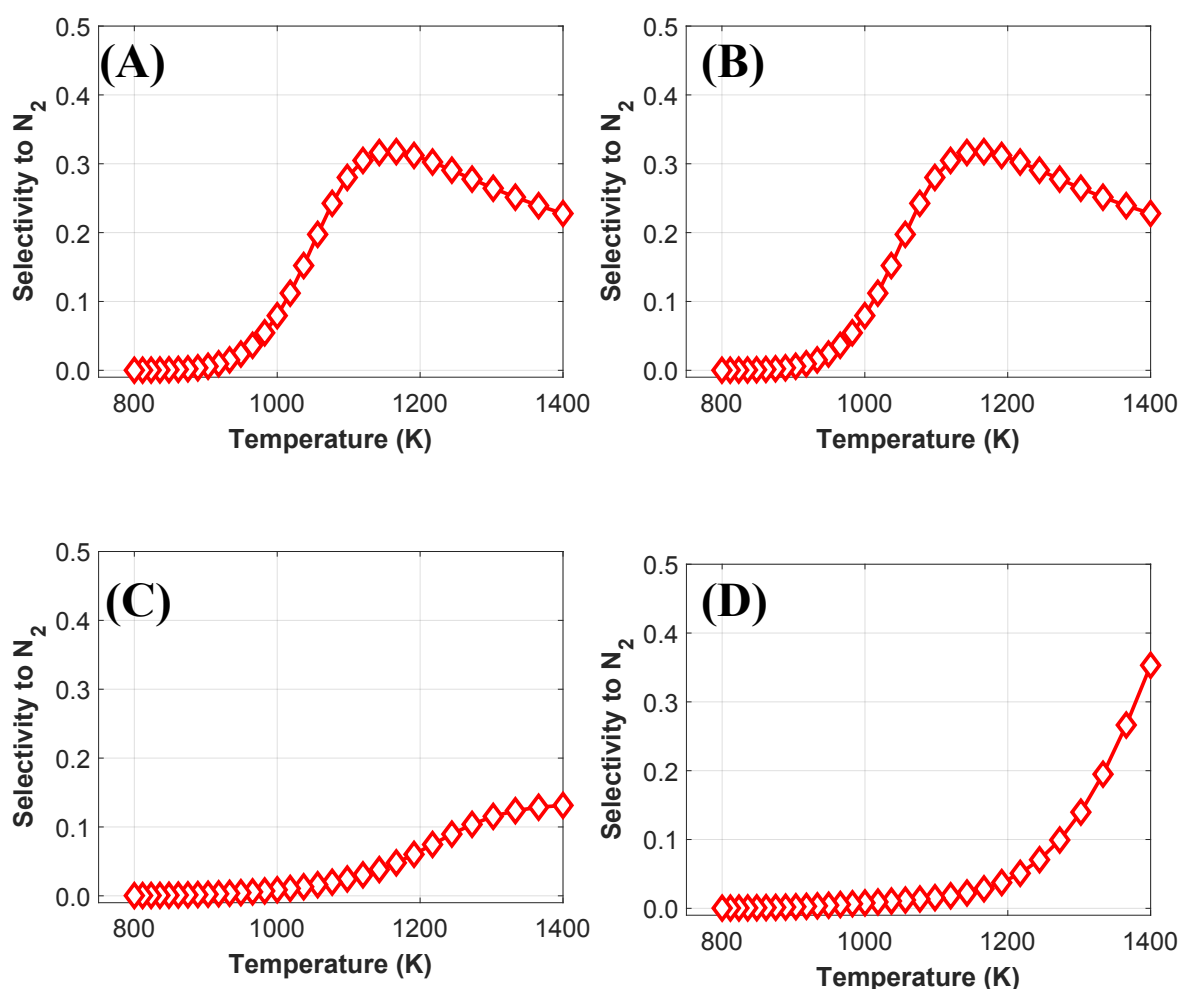


Figure S12. Predicted selectivity to N₂ after setting a large activation barrier (i.e. 2.5 eV) for (A) the formation of N₂* on Ni*; (B) the dimerization reaction on Ni*; (C) the direct dissociation of NO* on Ni*; and (D) the formation of N₂O* on Ni*

10. Sites involved in surface reactions over Ni/Cu bimetallic alloys

Several elementary events in our microkinetic model involve two sites, which may be of different type on the Ni/Cu bimetallic alloys. On the latter surfaces, the two-site reactions (see Table 2) can happen either on Cu sites, where the reactants and products are on Cu*, or on pair of sites that include both Ni* and Cu*. Table S3 tabulates the two-site events of the NO + CO reaction along with the site types whereon the reactant and product adspecies are adsorbed in our model.

Table S3. Two-site events and sites where reactant and product species are adsorbed. The adsorption sites (i.e. either Ni* or Cu*) are shown in bold. Also in bold are the reaction numbers, which correspond to the numbers shown in Table 2 in the main text. Empty sites are denoted as Ni* or Cu*. For occupied sites, the adsorbate is specified followed by the site type in parenthesis.

Reaction	Reactant 1	Reactant 2	Product 1	Product 2
$\text{NO}^* + * \leftrightarrow \text{N}^* + \text{O}^*$				
(R8)	$\text{NO}^* (\mathbf{Ni}^*)$	\mathbf{Cu}^*	$\text{N}^* (\mathbf{Ni}^*)$	$\text{O}^* (\mathbf{Cu}^*)$
$\text{NO}^* + \text{N}^* \leftrightarrow \text{N}_2\text{O}^* \eta 2\text{NbNt} + *$				
(R9)	$\text{NO}^* (\mathbf{Ni}^*)$	$\text{N}^* (\mathbf{Cu}^*)$	$\text{N}_2\text{O}^* \eta 2\text{NbNt} (\mathbf{Ni}^*)$	\mathbf{Cu}^*
$\text{N}_2\text{O}^* \eta 2\text{NtOt} + * \leftrightarrow \text{N}_2^* + \text{O}^*$				
(R12)	$\text{N}_2\text{O}^* \eta 2\text{NtOt} (\mathbf{Ni}^*)$	\mathbf{Cu}^*	$\text{N}_2^* (\mathbf{Ni}^*)$	$\text{O}^* (\mathbf{Cu}^*)$
$\text{N}_2\text{O}^* \eta 2\text{NbNt} + * \leftrightarrow \text{N}_2^* + \text{O}^*$				
(R13)	$\text{N}_2\text{O}^* \eta 2\text{NbNt} (\mathbf{Ni}^*)$	\mathbf{Cu}^*	$\text{N}_2^* (\mathbf{Ni}^*)$	$\text{O}^* (\mathbf{Cu}^*)$
$\text{CO}^* + \text{O}^* \leftrightarrow \text{CO}_2^* + *$				
(R14)	$\text{CO}^* (\mathbf{Ni}^*)$	$\text{O}^* (\mathbf{Cu}^*)$	$\text{CO}_2^* (\mathbf{Ni}^*)$	\mathbf{Cu}^*
$\text{NO}^* + \text{NO}^* \leftrightarrow \text{N}_2\text{O}^* \eta l + \text{O}^*$				
(R15)	$\text{NO}^* (\mathbf{Ni}^*)$	$\text{NO}^* (\mathbf{Cu}^*)$	$\text{N}_2\text{O}^* \eta l (\mathbf{Ni}^*)$	$\text{O}^* (\mathbf{Cu}^*)$
$\text{N}^* + \text{N}^* \leftrightarrow \text{N}_2^* + *$				
(R16)	$\text{N}^* (\mathbf{Ni}^*)$	$\text{N}^* (\mathbf{Cu}^*)$	$\text{N}_2^* (\mathbf{Ni}^*)$	\mathbf{Cu}^*

11. Computed adsorption energy for N_2O^* using different vdW functionals

Table S4 tabulates the $E_{ads}(\text{N}_2\text{O})$ for the three different adsorption geometries that are considered in the microkinetic model, computed using different exchange-correlation (XC) functionals, in particular: optPBE–vdW, optB86b–vdW, BEEF–vdW, and the Tkatchenko–Scheffler method (DFT–TS). Our results suggest that binding strengths that are predicted by different XC vdW functionals are considerably different, and this a known and non-trivial challenge in DFT calculations where nonlocal effects are accounted for.³ Therefore, the result of microkinetic simulations will strongly depend on the performance of the selected XC functional. For example, for the NO + CO reaction, one should expect that the selectivity peak of Figure 7 (A) will be higher than 0.65 if optPBE–vdW is used. By contrast, values of 0.25 or less can be expected if the DFT–TS or BEEF–vdW are employed.

Table S4. Cu lattice constants and N_2O^* adsorption energies (in eV) using different vdW treatments. Adsorption energies are presented only for the three N_2O^* geometries that are taken into account in the microkinetic model of the NO + CO reaction and are computed on the $\text{Ni}_2\text{Cu}(111)$ surface. Lattice constants are reported in Å and the experimentally determined value is 3.596 Å.

XC Functional	$E_{ads}(\eta 1)$	$E_{ads}(\eta 2NbNt)$	$E_{ads}(\eta 2NtOt)$	Lattice Constant
				(Cu)
optPBE–vdW	-0.93	-0.91	-0.95	3.648
optB86b–vdW*	-0.67	-0.74	-0.68	3.608
DFT–TS	-0.40	-0.56	-0.48	3.635
BEEF–vdW	-0.33 ± 0.14	-0.17 ± 0.23	-0.24 ± 0.31	3.661

* used functional in this work

References

- 1 J.-F. Paul, J. Pérez-Ramírez, F. Ample and J. M. Ricart, *J. Phys. Chem. B*, 2004, **108**, 17921–17927.
- 2 M. E. Bartram and B. E. Koel, *Surf. Sci.*, 1989, **213**, 137–156.
- 3 S. Gautier, S. N. Steinmann, C. Michel, P. Fleurat-Lessard and P. Sautet, *Phys. Chem. Chem. Phys.*, 2015, **17**, 28921–28930.